Joakim Enger Fredrikstad

Corrosion Fatigue of AA6082 Aluminium Alloy: The Effects of Coating and Ti Additions

June 2019

NTNU
Norwegian University of
Science and Technology

Master's thesis

2019

Joakim Enger Fredrikstad

Master's thesis

NTNU
Norwegian University of
Science and Technology
Faculty of Natural Sciences
Department of Materials Science and Engineering

NTNU
Norwegian University of
Science and Technology

NTNU
Norwegian University of
Science and Technology

Corrosion Fatigue of AA6082 Aluminium Alloy: The Effects of Coating and Ti Additions

Joakim Enger Fredrikstad

Materials Science and Engineering
Submission date: June 2019
Supervisor: Ola Jensrud
Co-supervisor: Lars Lodgaard
Hans Jørgen Roven

Norwegian University of Science and Technology
Department of Materials Science and Engineering

Abstract

The effects of anodising and an organic coating (KTL) on the corrosion fatigue properties of an extruded AA6082 aluminium alloy were investigated. Uncoated and anodised samples with extra Ti in the alloy were also tested. A component used in the suspension system of automobiles was approximated by test samples, all heat-treated to the T6x condition. Fatigue tests of all sample types were conducted both in air and in 5 wt% NaCl, in the high cycle fatigue regime, at R=-1. Mechanical properties, coating thickness, grain structure and surface roughness were also examined.

No significant effects of Ti additions were found either for samples fatigue tested in air or in 5 wt% NaCl. For anodised samples, however, a decrease in fatigue life was observed for samples tested in both atmospheres. The brittle oxide layer in the surface was assumed to have cracked early during cyclic loading, which caused stress concentrations that accelerated crack initiation. The observed effects of coating with KTL were more promising. Increased fatigue life was demonstrated, both in air and in 5 wt% NaCl. An increase in fatigue life of 413 % relative to uncoated samples was found in corrosion fatigue. Increased corrosion fatigue life was found even for samples with scratched KTL coatings. In addition to insulating the metallic surface from the corrosive solution, it was suggested that the ductile coating decreased the surface stress concentration of the aluminium, thus impeding crack initiation. Coating of the component with KTL was recommended.

Sammendrag

Effektene av anodisering og organisk belegg (KTL) på korrosjonsutmattingsegenskapene til en ekstrudert AA6082 aluminiumslegering ble undersøkt. Ubelagte og anodiserte prøver med ekstra Ti i legeringen ble også testet. En komponent brukt i hjulopphenget til biler ble tilnærmet med prøvestaver, som alle var varmebehandlet til T6x-tilstand. Utmattingstester av alle prøvetyper ble gjennomført både i luft og i 5 wt% NaCl, i høysykelutmattingsregimet, med R=-1. Mekaniske egenskaper, beleggtykkelse, kornstruktur og overflateruhet ble også undersøkt.

Ingen betydelige effekter av Ti-tillegg ble funnet hverken for utmattingsprøver testet i luft eller i 5 wt% NaCl. For anodiserte prøver, derimot, ble redusert utmattingsliv observert for prøver testet i begge atmosfærer. Det sprøe oksidbelegget i overflaten ble antatt å ha sprukket tidlig under syklisk spenningsbelastning, hvilket skapte spenningskonsentrasjoner som aksellererte sprekkinitiering. De observerte effektene av belegning med KTL var mer lovende. Økt utmattingsliv ble demonstreft, både i luft og i 5 wt% NaCl. En økning i utmattingsliv på 413 % relativt til ubelagte prøver ble funnet i korrosjonsutmatting. Økt korrosjonsutmattingsliv ble observert selv for prøver med oppripet KTL-belegg. I tillegg til å isolere den metalliske overflaten fra den korrosive løsningen, ble det antatt at det duktile KTL-belegget reduserte spenningskonsentrasjonen i aluminiumoverflaten, og dermed bremset sprekkinitiering. Belegning av komponenten med KTL ble anbefalt.

Preface

This master's thesis was performed at the Department of Materials Science and Engineering at the Norwegian University of Science and Technology (NTNU). This thesis was conducted during the spring of 2019, and it is a direct continuation of a project work done in the fall of 2018. Some parts have been reused. The aim of this thesis was to investigate the corrosion fatigue properties of an aluminium 6082 alloy with and without Ti additions, and with and without anodising and an organic coating.

I would like to thank my supervisor, Ola Jensrud, and my co-supervisors, Lars Lodgaard and Hans Jørgen Roven, for professional guidance throughout this thesis. I also need to thank SINTEF for supply of reference data, and Benteler Automotive both for supplying material, and for giving me confidence by accepting me for a permanent position once the thesis is completed. For assistance and training in the metallurgical laboratory, the mechanical laboratory and the electron microscopy laboratory, I would like to thank Berit Vinje Kramer, Pål Christian Skaret and Yingda Yu, respectively. Finally, I want to express my gratitude to my wife, Miriam Enger Fredrikstad, for her unwavering patience during hectic times, and for providing the motivation necessary to finish this thesis on time.

This thesis was done in accordance with the regulations at the Department of Materials Science and Engineering at the Norwegian University of Science and Technology.

Trondheim, June 2019.

Joakim Enger Fredrikstad.

Table of Contents

Abbreviations

ϵ	Engineering strain
σ	Engineering stress
σ_a	Stress amplitude
σ_u	Ultimate tensile stress
σ_y	Yield stress
σ_{max}	Maximum stress
%AR	Percent plastic areal reduction at fracture
%EL	Percent plastic elongation at fracture
CT	Coating thickness
D	Depth of field
E	Young's modulus
EBSD	Electron backscatter diffraction
ED	Extrusion direction
GS	Grain size
IGC	Intergranular corrosion
KTL	Cathodic electrophoretic coating
N_f	Number of cycles to failure
R	Stress ratio
R_a	Average roughness of profile
R_{max}	Maximum peak to valley height of roughness profile within a sampling length
SD	Short transverse direction
SEM	Scanning electron microscope
STD	Standard deviation
TD	Long transverse direction

1. Introduction

A metal subjected to cyclic stress conditions may experience failure at a stress much lower than that required to cause fracture at a single application of load [1]. This phenomenon is called fatigue, which is a field of great importance. The mechanisms of fatigue may be further complicated by the presence of a corrosive environment, and the simultaneous exposure to cyclic stress and corrosion is called corrosion fatigue [2]. Fatigue failures, in general, are hard to predict. Consequently, there are several examples of fatigue failures with catastrophic consequences, in applications such as aeroplanes, bridges and oil rigs. A well-known example of the latter is the Alexander Kielland platform [3].

Aluminium is a metal that may suffer from both corrosion and fatigue. It is extensively used in the automobile industry due to its high strength to weight ratio [4], which allows for a lighter car and, consequently, lower fuel consumption [5]. When aluminium is used in the suspension of the car, it is exposed to a corrosive cyclic stress environment, and corrosion fatigue needs to be accounted for [6]. Any sudden failure related to the suspension of the car could render steering impossible, which might endanger human lives. It is therefore important to understand the corrosion fatigue properties of aluminium, especially in suspension system applications.

The influence of corrosion on fatigue may be minimised by alloying additions, and by the application of a protective coating on the surface [7]. However, some coatings may still negatively impact the corrosion fatigue properties [8]. This thesis aims to investigate the effects of coating and Ti additions on an extruded aluminium 6082 alloy. The alloy is presently used in the suspension system of cars, through a component that is extruded, heat-treated to T6x while retaining its extruded microstructure, and mechanically formed. The corrosion fatigue properties of the component are investigated through test samples exposed to tensile stress cycles while submerged in saltwater. The effects of both anodising and an organic coating are investigated.

2. Theory

This chapter introduces theory that is important to understand when working with fatigue and corrosion fatigue of aluminium.

2.1 Mechanical Properties of Metals

Basic mechanical properties of metals can be found from tension tests. A sample is stressed in increasing tension until fracture occurs, while force and elongation are measured. The engineering stress (σ) is calculated from Equation 2.1, and the engineering strain (ϵ) from Equation 2.2.

$$\sigma = \frac{F}{A_0} \tag{2.1}$$

$$\epsilon = \frac{\Delta L}{L_0} \tag{2.2}$$

Here, F is the nominal force applied, A_0 is the cross-section area before deformation, ΔL is the resulting elongation and L_0 is the length before deformation [9].

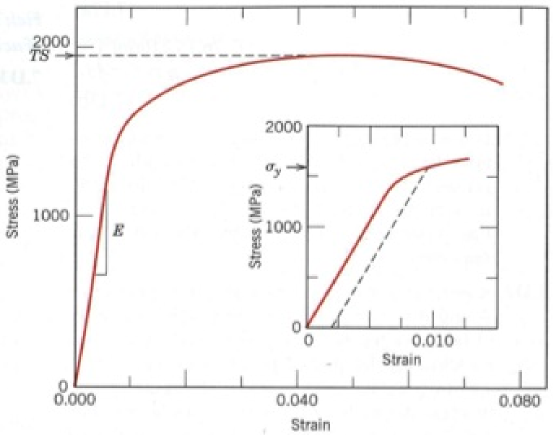

Figure 2.1: Stress-strain curve for a ductile material. Indicates how the curve is used to find elastic modulus (E), yield stress (σ_y) and tensile strength (TS) [9].

The resulting stress and strain values are plotted against each other in a stress-strain curve, as shown in Figure 2.1. Several material properties can be read from this curve. The yield stress (σ_y) can be found as the transition between the linear and the non-linear regimes of the curve, the point where strain goes from elastic (reversible) to plastic (irreversible). This transition is usually a gradual one, so the stress that gives 0.2 % plastic deformation is used in practice. The elastic modulus (E), which is connected to the strength of atomic bonds in the material, can be found as the slope of the linear part. The maximum stress of the curve is termed tensile strength or ultimate tensile stress (TS, or σ_u). The ductility is measured by maximum elongation and areal reduction. Maximum elongation is measured by the percentage of plastic strain at fracture, as shown in Equation 2.3, and the areal reduction is found from Equation 2.4.

$$\%EL = \left(\frac{l_f - l_0}{l_0}\right) \times 100 \tag{2.3}$$

$$\%AR = \left(\frac{A_0 - A_f}{A_0}\right) \times 100 \tag{2.4}$$

Here, l_f is the length after fracture, l_0 is the original length, A_0 is the cross-section area before elongation and A_f is the corresponding area after fracture [9].

2.2 Aluminium

Aluminium is a light metal, with a density of only 2.70 g/cm^3. The specific strength (strength per weight) of its alloys exceeds that of steel, which can be exploited in manufacturing lighter products of equal strength. Because of this, aluminium alloys enjoy great popularity in aeroplanes, cars, and lightweight constructions [4, 10].

2.2.1 Alloying Systems

Pure aluminium is relatively soft, with a tensile strength of 70-100 MPa. A significant increase in strength may be achieved by alloying aluminium, most commonly with Si, Mn, Mg, Cu and/or Zn [4]. Wrought aluminium alloys are classified by the main alloying elements, as shown in Table 2.1.

6xxx-Series

The 6xxx-series alloys are mainly alloyed with Mg (0.5-1.3%) and Si (0.4-1.4%) [4]. Some other common alloying elements and their effects are given in Table 2.2. The effects of Ti are given below.

Table 2.1: Al alloying series [4, 5].

Series	Main alloying elements
1xxx	None (pure Al)
2xxx	Cu
3xxx	Mn
4xxx	Si
5xxx	Mg
6xxx	Mg+Si
7xxx	Zn(+Mg)
8xxx	Others

Table 2.2: Secondary alloying elements in the 6xxx-series [4].

Alloying element	Effect
Mn (0.5-0.7)%	Grain refining.
Cr (0.1-0.3)%	Grain refining.
Cu(0.3-0.9)%	Gives increased strength. More than 0.5% Cu gives reduced resistance to corrosion.

The Effects of Alloying with Titanium

Titanium has been reported to act as a grain refiner in both cast alloys [11] and wrought 6xxx alloys [12]. It was shown for 6061-alloys that Ti causes refinement of the microstructure, and induces dispersion of precipitates. Ti alone forms $TiAl_3$, which acts as precipitation points for primary aluminium dendrites. More frequent dendrite nucleation or initiation gives more and smaller grains. Grain refinement was enhanced further by Ti reacting with B in the alloy to form TiB_2. These particles, together with $TiAl_3$, are more effective grain refiners than $TiAl_3$ alone [13].

Ti has also been shown to increase machinability in 6061. Refinement of intermetallic particles such as $CuAl_2$ and Mg_2Si induces breaking of the scrap made during machining, frequently termed chips. This contributes to an optimised cutting process, as small and brittle chips make it easier to extract chips away from the cutting front, impeding the formation of a built-up edge on the cutting edge of the tool [14].

The 6082 Alloy

The chemical composition of the different alloying elements that define the 6082 alloy are shown in Table 2.3, while Table 2.4 shows some mechanical properties of the 6082 alloy in its T6 condition.

Table 2.3: Common chemical composition of the 6082 alloy [5].

Alloying element	Si	Fe	Cu	Mn	Mg	Zn	Cr	Ti
Percentage (wt %)	0.70-1.3	0.50	0.10	0.40-0.10	0.60-1.0	0.20	0.25	0.10

Table 2.4: Mechanical properties of 6082 [15–18].

Modulus of elasticity, E [GPa]	69-70
Yield Strength, σ_y [MPa]	240-270
Tensile Stress, σ_u [MPa]	290-310

2.2.2 Heat Treatment

Heat treatment in aluminium alloys is a way of increasing their strength and hardness. The precipitation of uniformly dispersed hardening particles in the matrix material inhibits dislocation movement and plastic deformation. This hardening mechanism is called precipitation hardening. It is a two-part process, where solution heat treatment is followed by precipitation heat treatment [19]. The process is shown graphically in Figure 2.2.

Solution Heat Treatment

Solution heat treatment is the first step of the precipitation hardening process. The alloy is heated to a temperature in a single-phase area of the phase-diagram and held at that elevated temperature until all alloying elements go into solid solution. This is followed by quenching, to ensure that no precipitation of secondary phases occurs. The resulting supersaturated state of the material is relatively stable, due to low diffusion rates at low temperatures [19].

Precipitation Heat Treatment

The second step of the precipitation hardening process is precipitation heat treatment, which is also called artificial ageing. The alloy is heated to an intermediate temperature, where diffusion times are lower. Here, alloying elements will form precipitates, which will gradually transform into a stable secondary phase. The desired precipitates, however, are metastable and form earlier in the heat treatment. These precipitates give the optimal combination

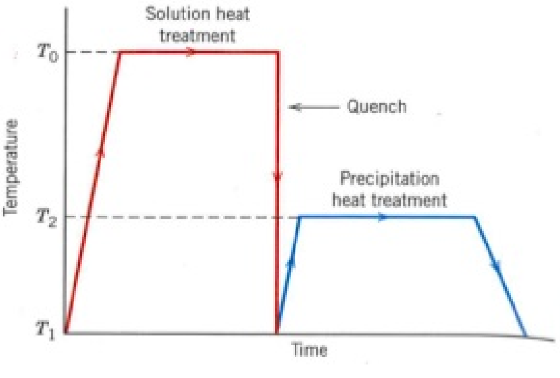

Figure 2.2: Temperature versus time for precipitation hardening [19].

of size and dispersion, which yields the best hardening contribution. An alloy where the stable phase has been allowed to form is called over-aged. When the desired precipitates are formed, the alloy is cooled to room temperature [19].

Heat Tempers

Solution heat-treated alloys where the strength after a few weeks is relatively stable are given the temper T. This is followed by one or more numbers, which contain information about a sequence of basic treatments given to the alloy [20]. The different tempers are described in Table 2.5.

Table 2.5: An explanation of the different heat treatments and their temper designations [20].

Temper	Explanation
T1	Cooled from an elevated-temperature shaping process and naturally aged to a substantially stable condition
T2	Cooled from and elevated-temperature shaping process, cold-worked, and naturally aged to a substantially stable condition
T3	Solution heat-treated, cold-worked, and naturally aged to a substantially stable condition
T4	Solution heat-treated and naturally aged to a substantially stable condition
T5	Cooled from an elevated-temperature shaping process and artificially aged
T6	Solution heat-treated and artificially aged
T7	Solution heat-treated and over-aged or stabilised
T8	Solution heat-treated, cold-worked, and artificially aged
T9	Solution heat-treated, artificially aged, and cold-worked
T10	Cooled from and elevated-temperature shaping process, cold-worked, and artificially aged

2.3 Corrosion of Aluminium

Aluminium is highly reactive and has a high affinity for oxygen. However, aluminium does not suffer from general corrosion in most atmospheres. This is because a chemically inert Al_2O_3-film forms rapidly on the metal surface, reaching a thickness of about 1 nm in seconds. The protective oxide film impedes corrosive reactions by forming a physical barrier between the aluminium and the atmosphere. The properties of the oxide include resistance to dissolution and electrical insulation. This means that further aluminium oxidation can not happen in combination with cathodic reactions on the oxide surface. The stability of the oxide film, represented as potential versus pH, is illustrated in Figure

2.3. This shows that aluminium is passive in a pH-range from about 3 to 12 (depending on the activity of aluminium ions in solution) [7].

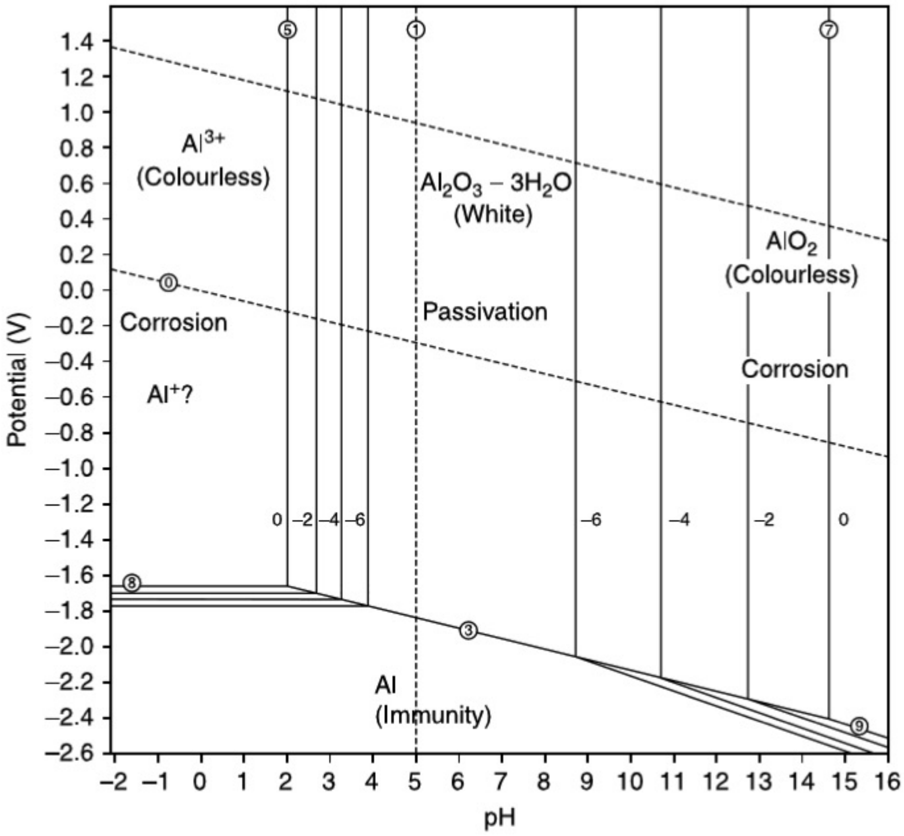

Figure 2.3: Pourbaix diagram for pure aluminium [7].

Even though aluminium is passive and in most atmospheres do not suffer from general corrosion, it might still suffer from localised corrosion such as pitting and intergranular corrosion (IGC). These forms of corrosion are explained in the following subchapters.

2.3.1 Pitting

The most common form of corrosion for aluminium is pitting. Pitting results from local damages in the protective oxide layer, such that corrosion might happen on small exposed areas of the metallic surface. The pits originate from the top of a horizontal surface, and penetrate vertically into the material [21].

When local corrosion first occurs, the corrosive reaction will lead to local acidity, thus hindering the re-formation of the oxide layer. Such local defects in the protective layer are usually facilitated by chlorides, through the formation of $AlCl_3$-particles. These serve as cathodes in microgalvanic cells, where the exposed aluminium surface is the anode.

Aluminium ions released from the surface form aluminium hydroxide compounds, which increase the local acidity, causing sustained pitting of the metal [7].

The potential for pitting in aluminium alloys depend upon its alloying elements. For example, pitting potential has been shown to decrease for Zn-content up to 3 wt%, and to increase dramatically for Cu-content up to 5 wt% [22].

2.3.2 Intergranular Corrosion

Intergranular corrosion (IGC) occurs along the grain boundaries of some alloys, as a result of precipitate-depleted regions. During heat treatment, precipitates migrate to grain boundaries, effectively depleting the immediately adjacent areas [21].

Generally, the driving force for IGC is the difference in electrochemical potential between the grain boundary precipitates and the bulk, or the adjacent microstructure. As shown in Figure 2.4, the solid solution zone, or the bulk, will interact with the zone that has been depleted of solutes (solute depleted, also called precipitate free zones or PFZ). The grain boundary precipitates may also interact with the solute depleted zone. Which mechanisms govern intergranular corrosion depends on the alloy.

In aluminium-copper alloys, the precipitation of Al_2Cu-particles leaves the PFZ anodic relative to the solid solution, exposing the immediately adjacent solid solution to corrosion. In aluminium-magnesium alloys, the situation is different, as the precipitating Mg_2Al_3-particles are less noble than the PFZ. Consequently, the precipitates on the grain boundaries will suffer from corrosion attacks [7, 23]. In 6xxx-alloys that contain Cu, IGC is caused by precipitation of Q-phase ($Al_5Cu_2Mg_8Si_6$). The Q-phase precipitates on the grain boundary will be nobler than the PFZ, and corrosion will occur in the PFZ [24].

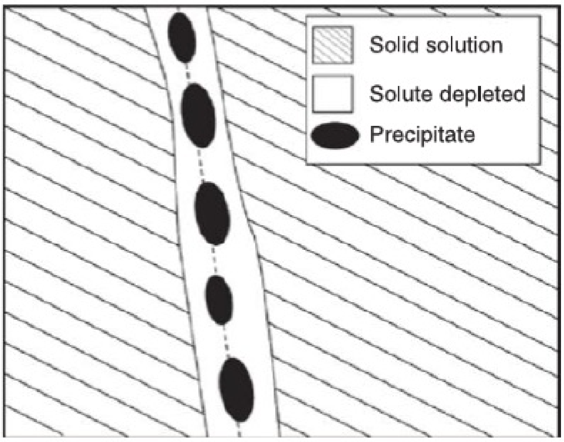

Figure 2.4: The phases participating in intergranular corrosion. [7]

2.4 Anodising

Anodising of aluminium is an electrochemical process where the naturally forming oxide layer is grown thicker to protect the bulk material. The aluminium substrate functions as the anode in an electrolysis cell, as this is where oxidation occurs. Other important elements in the anodising process are the cathode, the applied potential, and the electrolyte [25].

When a substrate is submerged in an electrolyte and connected to an external circuit, a steady-state process will establish, where aluminium ions are supplied by oxidation of the metal surface, and hydroxide and hydrogen ions are produced by hydrolysis of the electrolyte. The aluminium ions react with the hydroxide ions to form the oxide, while hydrogen ions are transported through the electrolyte to the cathode, where the cathodic hydrogen reduction reaction occurs. The electrolyte composition and concentration governs the conductivity in the circuit, but also the structure of the oxide layer. Thus, the electrolyte is an important parameter, that decides the efficiency of the anodising process [25].

The industrial process of anodising aluminium starts with pretreatment, cleaning and rinsing of the aluminium part. After this, the part is submerged in electrolyte and connected to an external power circuit. This is typically done at temperatures <30 °C. When the desired coating thickness has been achieved, post-treatments are required. The surface that has been in contact with the electrolyte is dissolved, and the surface is sealed. Adsorption and precipitation of reaction products from the sealing solution remain at the surface, increasing the corrosion resistance of the oxide. Sealing is typically done at about 90-100 °C [26].

2.5 Electrophoretic Deposition

Electrophoresis is an effect where charged powder particles dissolved in a liquid move as a result of an applied electric field [27]. The utilisation of this effect to deposit material onto a conductive substrate is termed electrophoretic deposition. Electrophoretic deposition must not be confused with electroplating, as the former relies upon the suspension of particles, and the latter on the solution of ionic species through the use of salts [28].

Electrophoretic deposition processes may be either anodic or cathodic. In the former, positively charged particles are deposited onto the negatively charged anode. Conversely, in the latter, negatively charged particles are deposited onto the positively charged cathode. As long as the surface charge of the particles can be modified, both types of deposition are possible [28].

There are principally two steps to the electrophoretic deposition process. The first is the transfer of charged powder particles through the solvent, by the process of electrophoresis. The second step is the deposition of these particles onto the charged electrode, i.e. the substrate to be coated, in the form of a compact film [29].

2.6 Surface Roughness

The entirety of all irregularities in the topography of a surface is called surface texture. Surface texture can roughly be divided into surface roughness and waviness. Surface roughness is the finer irregularities found on the surface, including those inherent from the production process. Waviness, on the other hand, describes more widely spaced irregularities. These may result from for example machine deflections or vibrations. Surface roughness is present within the wavy structure of a sample, such that waviness must be subtracted to find roughness, and vice versa [30].

Roughness is the finely spaced differences in height and depth that occurs along a surface. These surface irregularities may not be defined unambiguously by a single surface parameter. Therefore, a variety of standardised parameters are used to characterise surface roughness [31]. Some of these parameters are explained in Table 2.6, and defined mathematically in Equations 2.5 to 2.9. Corresponding parameters may be defined for waviness.

Table 2.6: Different surface roughness parameters and their explanations [32].

Symbol	Explanation
R_a	Average roughness of profile
R_q	Root-mean-square roughness of profile
R_z	Mean peak to valley height of roughness profile
R_t	Maximum peak to valley height of roughness profile
R_{max}	Maximum peak to valley height of roughness profile within a sampling length

$$R_a = \frac{1}{L}\int_0^L |z(x)|dx \tag{2.5}$$

$$R_q = \sqrt{\frac{1}{L}\int_0^L z(x)^2 dx} \tag{2.6}$$

$$R_z = \frac{\sum_{i=1}^{n} p_i + \sum_{i=1}^{n} v_i}{n} \tag{2.7}$$

$$R_t = z_{max} - z_{min} \tag{2.8}$$

$$R_{max} = max(p_i - v_i) \tag{2.9}$$

Here, L is the sampling length, z(x) is the height over mean height, n is the number of samples along the sampling length, p_i is the peak height at sample i, v_i is the valley depth at sample i, z_{max} is the highest peak in the sampling length and z_{min} is the lowest valley in the sampling length [32].

2.7 Fatigue

A metal subjected to a repetitive or fluctuating stress will fail at a stress much lower than that required to cause fracture on a single application of load. Such failures are called fatigue failures [1].

The following subchapters introduce some common expressions and the S-N curve, which is the most common way to represent the fatigue properties of an alloy. This is followed by an introduction to some factors that influence fatigue.

2.7.1 Stress Cycles

In fatigue, the maximum stress is defined as σ_{max}, and the minimum stress as σ_{min}. These variables are used to describe the stress ratio (R), the mean stress (σ_m) and the stress amplitude (σ_a), as shown in equations 2.10, 2.11 and 2.12, respectively.

$$R = \frac{\sigma_{min}}{\sigma_{max}} \tag{2.10}$$

$$\sigma_m = \frac{\sigma_{max} + \sigma_{min}}{2} \tag{2.11}$$

$$\sigma_a = \frac{\sigma_{max} - \sigma_{min}}{2} \tag{2.12}$$

2.7.2 The S-N Curve

The S-N curve is a plot of the stress (S, or σ) versus the number of cycles to failure (N, or N$_f$), with N_f usually given on a logarithmic scale. The stress on the y-axis can be either σ_a, σ_{max} or σ_{min} [1]. An example of an S-N curve is given in Figure 2.5, which also shows the meaning of the terms fatigue strength and fatigue life.

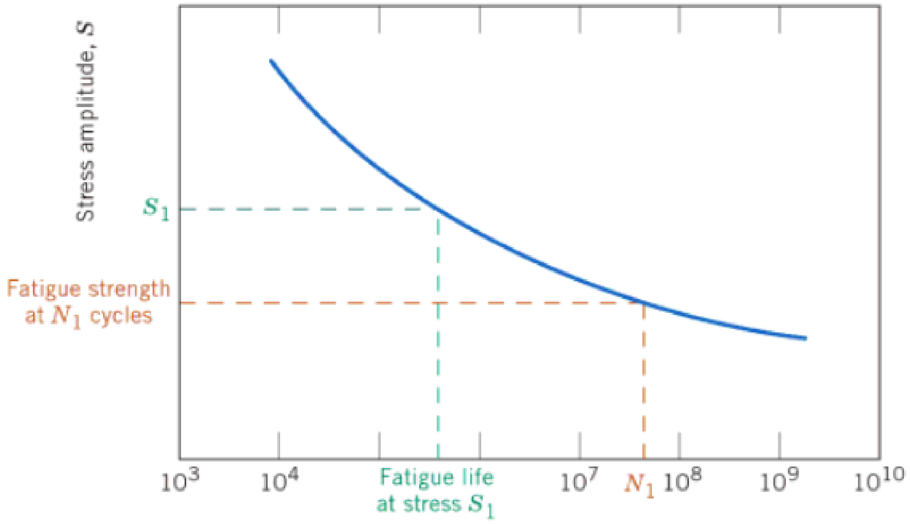

Figure 2.5: An S-N curve for a material that displays no fatigue limit. Indicates the meaning of fatigue strength and fatigue life [33].

The S-N curve is mostly used for high cycle fatigue, which is considered to be when the bulk of the metal is only deformed elastically for each cycle. This fatigue regime is mostly governed by crack initiation [34]. Low cycle fatigue is when each stress cycle introduces plastic strain in addition to the elastic. This fatigue regime is mostly governed by crack propagation [35]. The transition between these regimes is gliding, but it roughly corresponds to $N = 10^4$ cycles [1].

Some metals, like steel and titanium, experience a fatigue limit, a stress level below which the metal is assumed to be able to endure an infinite number of cycles without failure. This is seen in the S-N curve as a horizontal asymptote. For many nonferrous metals, like aluminium, the curve will not show such a limit. For these metals, the common practice is to define the fatigue strength as the stress at which the metal might endure a large number of cycles, as shown in Figure 2.5. Here, N_1 could indicate the chosen limit for number of cycles [1].

2.7.3 The Influence of Surface Roughness

Cracks during fatigue commonly initiate at the surface of the material. Tiny notches in the surface due to surface finishing will act as local stress raisers, which increase the rate of fatigue crack initiation. Thus, the manner of surface preparation during the manufacturing of the component is a factor that greatly influences the initiation of cracks during fatigue [36].

The highest numbers of cycles to failure are observed for smoothly polished samples, where any scratches are oriented parallel to the stress direction [1]. High-cycle fatigue life for carefully ground specimens, compared to smooth, is reduced by about 10 %, while normal machining may give a reduction of 20 % or more. Related factors such as residual surface stresses or other surface changes from processing may further influence fatigue [37].

2.7.4 The Influence of Coating

Coating of a component that is exposed to cyclic stresses may affect its resistance to fatigue. Cracks usually initiate in the surface of the component, so changes in surface properties, such as ductility, would be expected to influence fatigue properties. The effect depends, for example, on the difference in plastic properties between the substrate and the coating. If the coating has a lower yield strength than the substrate, then a crack tip in the coating has been shown to be partially shielded from the applied load. The substrate bears a greater part of the stress, leading to an inhibited crack growth rate in the coating. Conversely, if the coating has higher yield stress, the crack growth rate would be accelerated. This is only true, however, for the ideal case where coating and substrate have identical elastic properties. An elastic mismatch complicates the situation, and the difference between plastic mismatch and elastic mismatch dictates the resulting effect [38].

For the case of aluminium alloys with an anodised coating, the effect on fatigue properties has been shown to be detrimental. This is due to the brittle nature of the oxide layer on the aluminium surface. The combination of a coating that cracks easily when deformed, and adheres extremely well to the aluminium substrate, leads to an increased crack initiation rate. Reduced fatigue life is expected. The magnitude with which the crack initiation rate increases depends on the type of anodising process, the thickness of the applied oxide layer, and the substrate aluminium alloy and its pretreatment [8].

A number of other coating systems on aluminium have been investigated, leading to different results. An example of a coating that was found to improve fatigue and corrosion fatigue properties was a WC-10Co-4Cr coating, thermally sprayed onto an AA6063-T6 aluminium alloy. For this coating system, residual stresses in the coating from the deposition process were believed to cause the increased number of cycles to failure [39].

2.7.5 The Influence of Precorrosion

Both pitting and intergranular corrosion before fatigue will negatively impact fatigue properties. Such localised corrosive attacks may lead to severe stress concentrations locally at affected areas, effectively accelerating fatigue crack initiation. This will have a deleterious effect on the number of cycles to failure for a material subjected to cyclic loading [7].

The creation of pits prior to fatigue exposure will accelerate crack initiation through the notch effect, but fatigue of corroded metals must not be confused with corrosion fatigue. This is when corrosion occurs simultaneously to fatigue, effectively enhancing the reduction in fatigue strength, as described below [2].

2.7.6 Corrosion Fatigue

Corrosion fatigue is the combinative effect of corrosive environment and cyclic stress on a metal. The behaviour of metals exposed to corrosion fatigue differs significantly to those exposed to fatigue, and the fatigue strength is greatly reduced. A general rule proposed for aluminium automotive safety components is that the fatigue strength at 5×10^6 cycles to failure under constant amplitude loading is reduced by 50 %, and under variable amplitude loading by 20-25 % [40].

Generally, in corrosion fatigue, cracks initiate early in the fatigue life, growing gradually during fatigue exposure. Crack initiation may occur from metal exposed to corrosion by slip motion caused by the imposed stress, which becomes anodic compared to adjacent areas where slip does not occur. This leads to the formation of a local electrochemical cell, which serves to initiate pitting through anodic dissolution. As the pit grows, the stress concentration rises, until a crack is initiated. For some materials, it has been reported that intergranular corrosion occurs within primary pits, from which secondary pits arise in a complex interaction [41]. In addition to crack initiation, corrosion fatigue may influence the mechanisms of crack propagation, e.g. through crack tip wedging by corrosion products. Due to the great influence of corrosive attacks on corrosion fatigue, the corrosion resistance of the material in the relevant environment is generally the most influential factor on the fatigue strength [2].

2.7.7 The Influence of Loading Frequency

Initiation and growth of fatigue cracks may both be assisted by chemical reactions such as pitting or corrosion of the crack tip. This is most obviously the case when the material is exposed to some corrosive solution. For example, aluminium will experience shorter fatigue life in a saltwater solution than in air. However, even materials tested in air may, in some instances, be affected by the moisture and gases present in the air [7].

The magnitude with which these reactions affect the mechanisms of fatigue depends upon the time available for the reactions to transpire. Thus, samples tested at lower frequencies should be expected to experience a decrease in fatigue life compared to those tested at higher frequencies, the magnitude of which depends on the chemical properties of the material and the environment it is exposed to [42].

2.7.8 The Influence of Mean Stress

When cyclic loads are applied, the mean stress, expressed by R, is an important parameter. Completely reversed loading, corresponding to R=-1, represents the standard case where the mean stress is zero. When comparing different cycles with equal σ_{max}, the fatigue life is known to increase with increasing R. Empirical equations exist for computing corresponding stress amplitudes at R=-1 from non-zero mean stresses. A conservative example is the Smith Watson Topper (SWT) equation. This is shown in Equation 2.13,

$$\sigma_{ar} = \sqrt{\sigma_a \times \sigma_{max}} \tag{2.13}$$

where σ_{ar} is the corresponding stress amplitude for R=-1, σ_a is the stress amplitude at the non-zero mean stress, and σ_{max} is the largest stress at the non-zero mean stress [42]. This corresponding stress amplitude may be used to estimate the corresponding number of cycles to failure at R=-1 through the use of the Basquin law in the high cycle regime. This law is shown in Equation 2.14,

$$\sigma_{ar} = \sigma_f^{'}(2N_f)^b \tag{2.14}$$

where σ_f and b are material constants, that need to be estimated or found from tables [1].

2.7.9 The Influence of Loading Mode

Tensile stresses give uniform stress distributions throughout the cross-section. Bending loading, on the other hand, introduces unevenly distributed stresses. One side is in compression while the other is in tension, yielding a smaller effect on the material. Therefore, the number of cycles to failure is expected to be higher for materials exposed to bending than tension [43].

2.7.10 The Influence of Size

Components subject to bending stresses experience a fatigue limit that decreases with increasing size. Bending stress introduces a stress gradient that decreases rapidly for small samples. For larger cross-sections, however, the decrease in stress with depth is more gradual, and more material experiences high stress. This effect means that investigations based on smaller test samples overestimate the fatigue life of larger components [37, 43].

2.7.11 The Statistical Nature of Fatigue

Although S-N curves are usually given as definite solutions to the number of cycles for each stress amplitude of a specific material, it is important to emphasise the fact that these curves represent average values, and that significant deviations from the curves should be expected. As fatigue properties are statistical, a three-dimensional surface that gives the relationship between stress, number of cycles to failure and the probability of failure would be a more accurate representation. It is not known for certain which statistical distribution function accurately describes the distribution of fatigue life at a given stress amplitude, but it is frequently assumed to follow a normal distribution curve when the number of cycles to failure are given on a logarithmic scale [1].

2.8 Measuring Electronically

To measure the grain size in a micrograph, a common method is to divide the length of a straight test line by the number of grains spanned. This method is called linear intercept [44]. One way to measure test lines electronically is by the use of the program ImageJ [45]. Here, a scale is set by measuring the length of the known scale bar. This scale is then used to calculate the actual length of any other lines drawn on the image.

This program may also be used to measure the thickness of a coating. A number of test lines are drawn normal to the edge of the sample, through the coating and to the interface between coating and metal. The average length of these lines represents the coating thickness.

2.9 Scanning Electron Microscope

The scanning electron microscope (SEM) is a useful tool when characterising surfaces on a microscopic scale. The area of interest is irradiated by a thin electron beam. When the electrons interact with the sample, several detectable signals that might be used to characterise the surface arise. These include secondary electrons, backscattered electrons, characteristic X-rays and Auger electrons. These signals may give information regarding the sample's chemical composition, topography, crystallography, and more [46].

One major advantage of the SEM is its ability to view a large range of heights in focus simultaneously. This property is called depth of field. The depth of field (D) in SEM is calculated by Equation 2.15,

$$D = \left[\frac{\delta}{M} - d_p\right] \times \frac{a}{r} \tag{2.15}$$

where δ is the resolution of the eye, M is the magnification, d_p is the electron optical resolution, a is the working distance and r is the radius of the objective aperture [46].

When investigating fracture surfaces, it is practical to maximise the depth of field. Equation 2.15 shows that this can be achieved by maximising the working distance [46].

2.9.1 EBSD

The SEM might also be used to obtain information on the grain structure of a sample, through the electron backscatter diffraction (EBSD) detector. This method of grain structure analysis relies upon the analysis of diffraction patterns acquired by a stationary beam of electrons on the sample surface. Each crystal lattice plane uniquely diffracts backscattered electrons according to Bragg's law, and these may be used to construct an image of the grain structure. As the electrons penetrate typically only up to 50 nm of the specimen surface, high-quality surface polishing is necessary. This may be achieved for example by the use of vibration polishing, electropolishing or plasma etching.

Results are achieved by evaluating diffraction patterns, which is usually an automatic feature of the software. The result is a variety of charts and figures, the most useful of which is the orientation map. This shows the grain structure according to crystallographic orientation and phase while generating quantitative microstructural descriptors. A more detailed deliberation of the EBSD is referenced in the form of a tutorial review by Randle [47].

2.10 Fracture Characterisation

Fractures may be divided into ductile, brittle and fatigue fractures, though many more classifications exist. Microscopical examinations of fracture surfaces are required to determine the type of fracture [48]. The main fracture types are described below.

2.10.1 Ductile Fracture

Ductile fractures are associated with plastic deformation, which leads to necking (local constriction in the cross-section area [9]). The final fracture in ductile materials is often called rupture [49]. An extreme case of necking, where the material deforms to a point before rupture, is seen in Figure 2.7 (a). Figure 2.7 (b) shows the most common ductile fracture profile, where a moderate amount of necking is followed by rupture.

Microscopically, most ductile fracture surfaces may be characterised by the presence of dimples. Dimples are microvoids that form when ductile materials are exposed to stress [48]. Depending on the orientation of the fracture surface, dimples may appear either spherical, as in Figure 2.6 (a), or more elongated, as in Figure 2.6 (b).

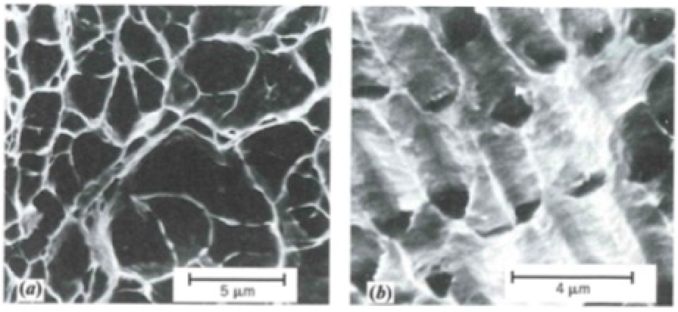

Figure 2.6: (a) Spherical dimples. (b) Elongated dimples [33].

2.10.2 Brittle Fracture

A fracture with little deformation and rapid crack propagation is characterised as brittle. Cracks in brittle materials propagate close to normal to the direction of applied stress, which usually yields a plane fracture surface [33]. A simple representation of a brittle fracture can be seen in Figure 2.7 (c).

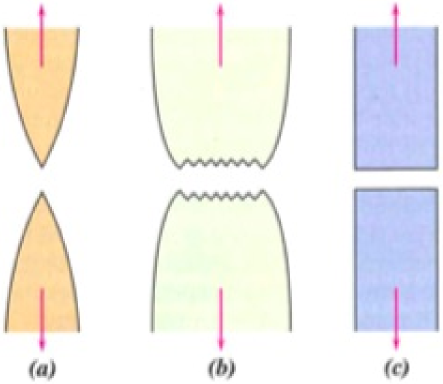

Figure 2.7: (a) Highly ductile fracture. (b) Ductile fracture with some necking. (c) Brittle fracture with no plastic deformation [33].

2.10.3 Fatigue Fracture

Fatigue fracture is the most common type of fracture. It occurs when cyclic stress of considerable size is applied to a material over time. The changing stress environment leads to local stress concentrations, which may lead to crack formations.

Fatigue cracks usually originate from the surface, growing from some local damage or irregularity. This will generally decide the appearance of the fracture surface, in both large and microscopic scale. The fracture mechanism may be divided into the following three stages [48].

Stage I - Crack Initiation

In the first stage, cracks initiate, typically at a free surface. For ductile materials, initiation may occur by the formation of slip bands, i.e. pile-up of dislocations that form cracks within grains. Materials of more limited ductility usually develop cracks at defects such as voids or inclusions [42]. These tiny cracks then grow along slip planes, typically in an angle 45° to the applied stress, penetrating only a few grains [48].

Stage II - Crack Propagation

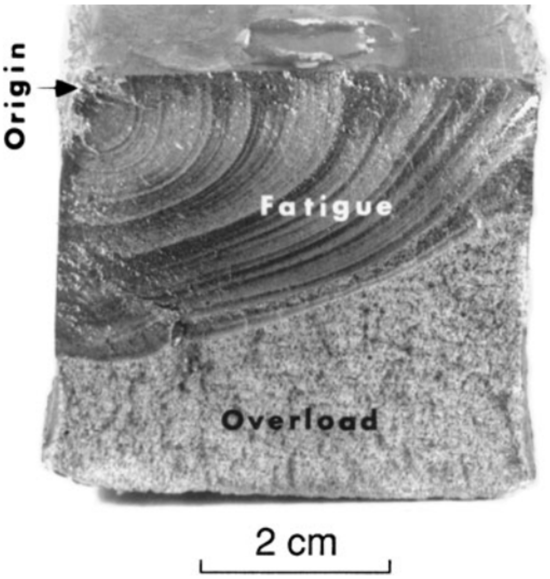

Figure 2.8: Beach marks on a brittle steel fracture surface [42].

The crack transitions from propagating along crystallographic planes to a plane that is fairly flat and approximately normal to the direction of the applied stress. This is the stage associated with fatigue crack growth. It can be seen macroscopically as a relatively smooth area close to the origin of the crack [42]. In this stage, the crack propagation may be either transgranular or intergranular. In transgranular fractures, the crack propagates through the grains, while in intergranular fractures, the crack propagates along the grain boundaries. The latter normally occurs as a result of grain boundary weakening processes and yields a fracture surface where the outline of the grains can be seen [33].

Stage III - Fracture

The cross-section of the material is greatly reduced, and the material can no longer bear the applied load. The residual fracture may be either ductile or brittle, depending on the material in question [48]. The final fracture area usually appears rough. Ductile materials may form a shear lip, oriented approximately 45° to the direction of applied stress [42].

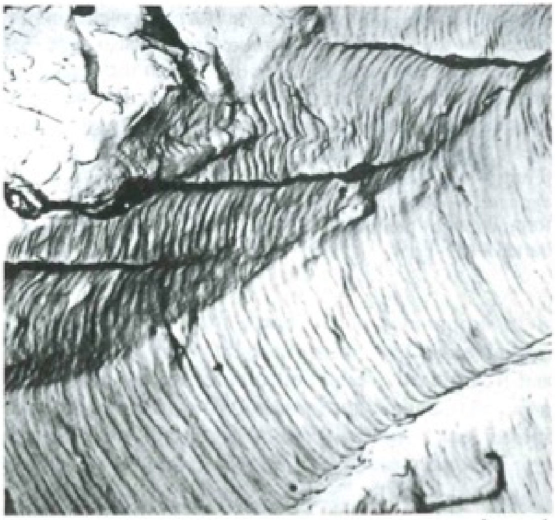

Figure 2.9: Striations in aluminium, image at 9000X magnification [33].

Characteristic Features

Some characteristics of fatigue fractures may be seen by the naked eye or by stereomicroscope, the most common of which is beach marks. These are a result of the variations in applied load combined with oxidised fracture surface [1, 42]. An example is shown in Figure 2.8. However, beach marks may not appear if the part has been loaded continuously [50].

By use of microscopes, one may see striations, as shown in Figure 2.9. These are parallel lines oriented perpendicular to the direction of crack growth, and the distance between them tend to increase with increasing crack length. Each striation is caused by crack tip blunting in a single stress cycle. Striations may be used to model crack growth, through the Paris law. This law is shown in Equation 2.16,

$$\frac{da}{dN} = (C\Delta K)^m \tag{2.16}$$

where $\frac{da}{dN}$ is the crack growth per stress cycle, ΔK is the stress intensity factor range and C and m are constants. Solving this expression leads to an equation which, once the striation spacing and crack size is known in two separate parts of the fatigue crack propagation area, may give an approximation of the number of cycles to failure [51].

Striations are generally more prominent for ductile materials [42, 48]. They may disappear over time, due to the formation of surface corrosion products. Also, both striations and beach marks may be damaged by surfaces rubbing against each other during stress cycling. Therefore, the absence of beach marks and striations does not exclude fatigue [33]. One last feature that may be used to understand the origin of the critical crack is ridge marks. These spread out radially from the crack origin, as shown in Figure 2.10 [52].

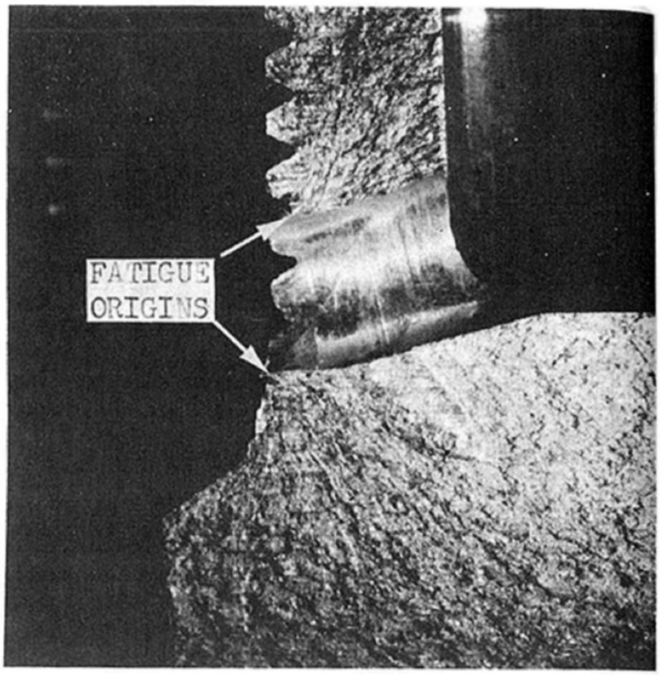

Figure 2.10: Ridge marks spreading from the two fatigue origins indicated [52].

3. Experimental

This chapter describes the material used in this thesis, some reference data supplied by SINTEF, some important results from previous work, and ultimately all experimental investigations that were executed.

3.1 Material

The samples used were of the aluminium alloy 6082. They were cut from a profile extruded by Benteler, of the same type that is usually processed into a part used in the suspension system of automobiles. Next, they were heat-treated to a variation of the T6 condition by SINTEF, simulating the heat treatment used by Benteler in the industrial process. This temper state is henceforth referred to as T6x. The approximate cross-sectional geometry of the extruded profile is shown in Figure 3.1, and the sample geometry is indicated in Figure 3.2. In both figures, the extrusion direction (ED), the short transverse direction (SD), and the long transverse direction (TD) are indicated.

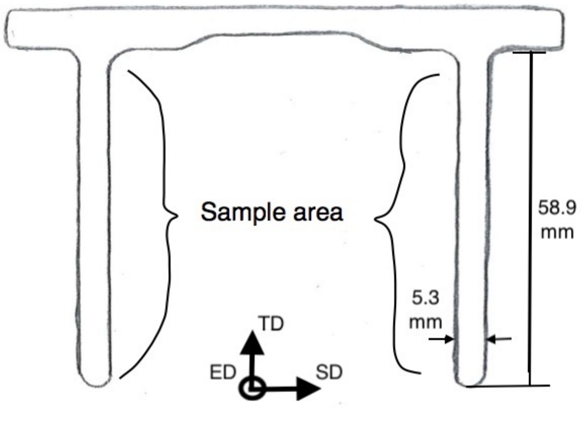

Figure 3.1: Cross-section geometry of the extruded profile from which the samples were made.

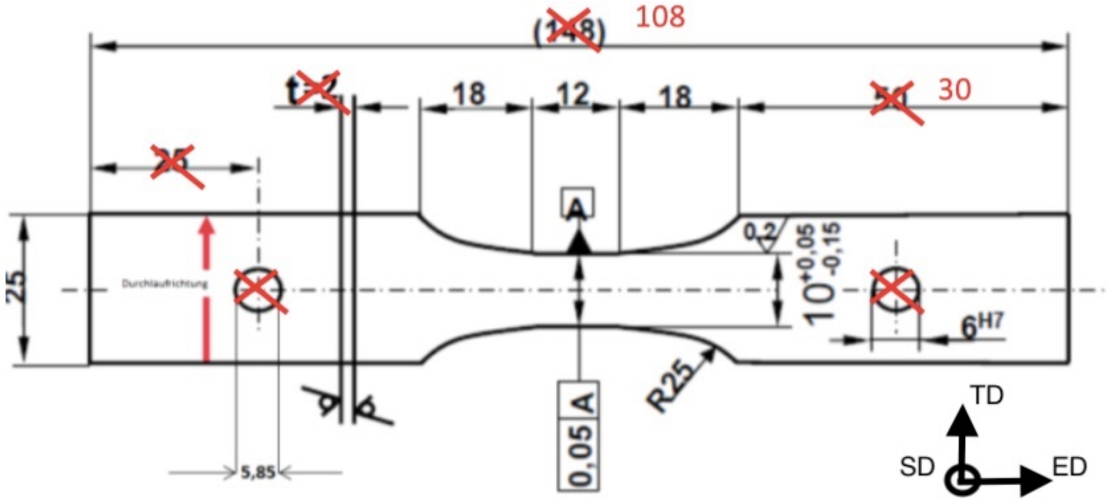

Figure 3.2: Geometry of the samples used. All dimensions are in mm. The thickness of the sample is 5.3 mm.

The samples were given different surface treatments. Some were left uncoated, some were anodised, and some were coated with an organic coating as described below. The anodised samples were treated by Hydal Aluminium Profiles, to a coating thickness specified to 11-13 µm. This coating was the same as the one used in the project work, as described in Chapter 3.3.

The organic coating was supplied by one of Benteler's divisions in Germany. This coating was applied with a process called KTL (Kathodische Tauchlackierung), which is assumed to be a cathodic electrophoretic coating process, and these samples will be referred to as KTL samples henceforth. The samples received a curing treatment at 160 °C for 20 min, and allegedly some pretreatment, but further details on the coating or coating process were not given.

Furthermore, some samples were supplied of a variation of the 6082 alloy with some extra Ti added. Half of these samples were anodised, while the other half were uncoated. The chemical composition of the alloy, both with and without extra Ti, are shown in Table 3.1. The values are nominal values of the 6082 alloy supplied by Benteler.

Table 3.1: Chemical composition of the used material.

Al alloy	Cr	Cu	Fe	Mg	Mn	Si	Ti
6082+Ti	0.15	0.001	0.17	0.63	0.55	0.91	0.09
6082	0.15	0.001	0.17	0.63	0.55	0.91	0.01

3.2 Reference Data

Fatigue test results were supplied by SINTEF, from a previous project on the fatigue properties of the 6082 alloy. All samples were as the one shown in Figure 3.2. Figure 3.3 shows results from fatigue tests in air. The series labelled pre cor 2h indicate samples that were exposed to a corrosive solution designed to trigger IGC, while the one labelled machined indicates that all edges of the samples were machined. All samples were tested with R=-1 and f=10 Hz.

The S-N curves in Figure 3.4 represent samples tested in 5 wt% NaCl with R=0.1 and f=5 Hz. These samples were given different surface finishes, indicated by the labels. Here, the series labelled machined w/smoothened edges in bend were machined only on the short edges as normal, and then ground in the bend to reduce surface roughness and impede crack initiation.

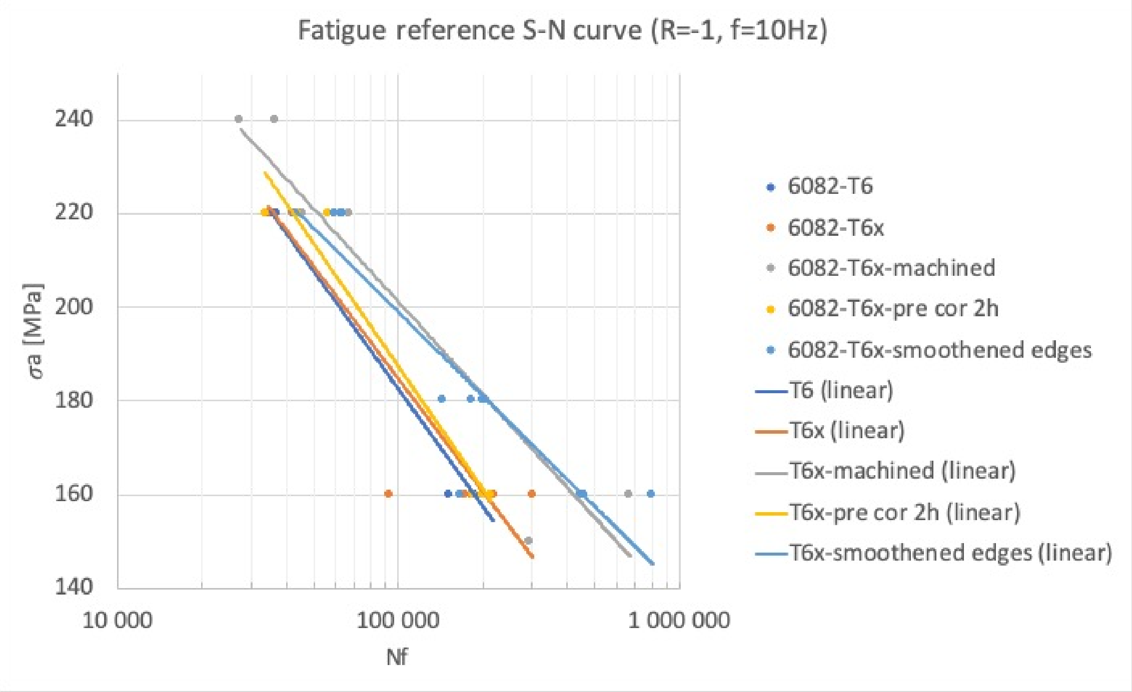

Figure 3.3: Fatigue results by SINTEF.

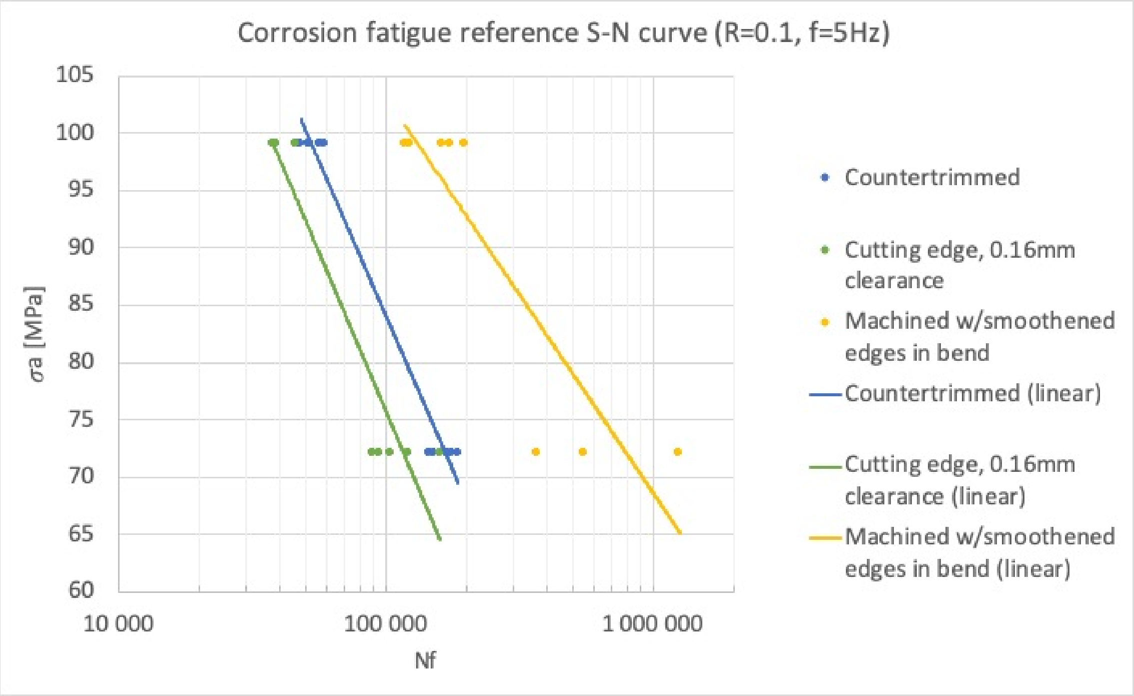

Figure 3.4: Corrosion fatigue results by SINTEF.

3.3 Results from Previous Work

The foundation for this master thesis was done in a project-work, entitled "The Effects of Anodising on the Fatigue Properties of Aluminium". Metallographic examinations of the uncoated and anodised samples were conducted therein, yielding the average grain sizes (GS) in the short transverse direction as shown in Table 3.2. Images of the grain structures of an uncoated and an anodised sample are regiven in Figure 3.6 (a) and (b), respectively. Table 3.2 also shows the results of tensile tests conducted on these samples, and the measured coating thickness (CT) of the anodised sample.

Furthermore, fatigue tests were done on uncoated and anodised samples, yielding the S-N curves shown in Figure 3.5. The results of fatigue tests done on samples that were exposed to a corrosive solution specified in ISO 11846 for 24 h and 96 h were also included. Note that these fatigue tests were done at only one value of σ_a, which is why no lines could be constructed for these samples.

Table 3.2: Mechanical properties and grain sizes.

	E [GPa]	σ_y [MPa]	σ_u [MPa]	%EL	%AR	GS [µm]	CT [µm]
Anodised	70.0	330	381	27.5	23.5	7.4	13.1
Uncoated	69.8	327	380	29.3	26.3	6.8	-

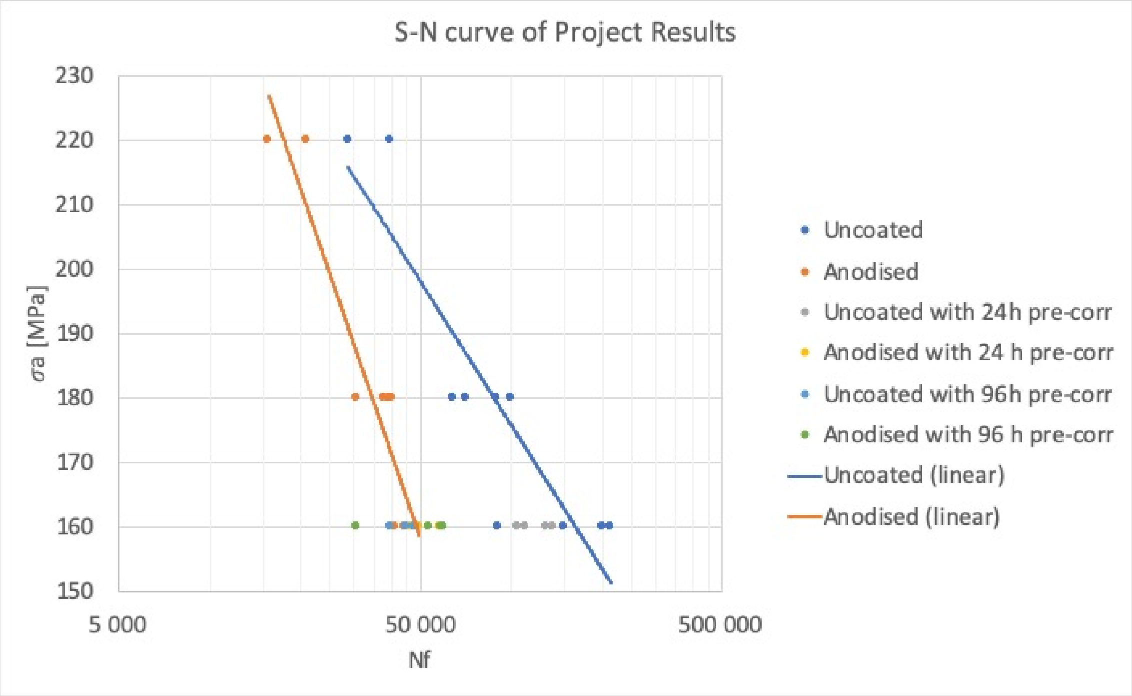

Figure 3.5: Results from fatigue tests done in project work.

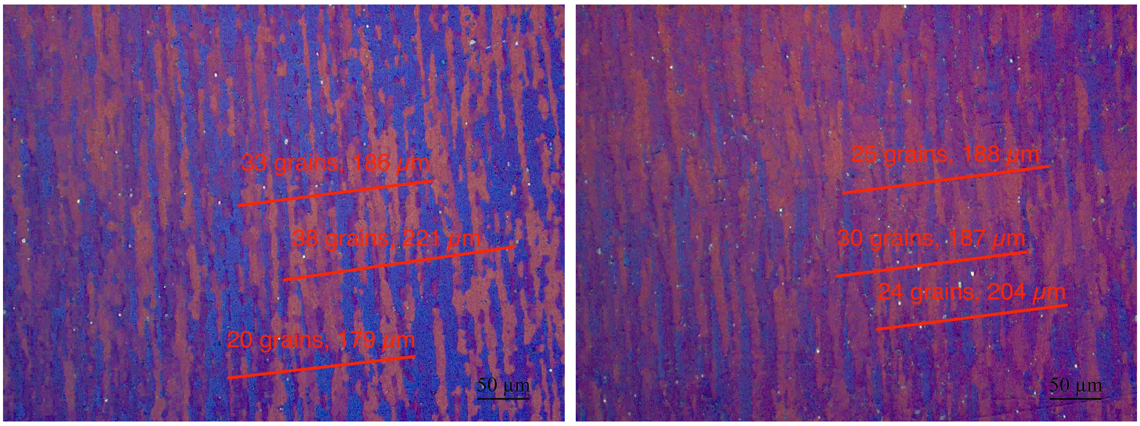

(a) (b)

Figure 3.6: Grain structures found in the project work from: (a) an uncoated sample, and (b) an anodised sample. Lines used to find average grain sizes in the SD are also included.

3.4 Test Methods

Grain structures, mechanical properties, surface roughness, fatigue and corrosion fatigue properties and fracture surfaces were all investigated, in the ways described below.

3.4.1 Metallography

One KTL-coated sample and one anodised Ti-containing sample were used for metallographic examinations. The samples were cut to suitable dimensions from the parallel area using Struers Discotom-5, exposing the plane consisting of the SD and the TD. Next, they were mounted into Epofix, ground and polished. Grinding was done using sandpaper with 240, 480, 800 and 2000 particles per square centimetre respectively, providing increasingly planar surfaces. Polishing was done at a Struers DP-U3 with diamond spray at 3 µm and 1 µm. The samples were rinsed with water between each grinding step, and washed with soap before and after each of the polishing steps.

After polishing, the polished surfaces were anodised. The anodising solution used was 5 % HBF_4, with an applied voltage of 20 V and time of 90 s. The samples were immediately rinsed with water and ethanol.

After anodising, the samples were examined in a Leica MEF4M light optical microscope. Pictures were taken of the grain structures, using polarised light, to measure grain sizes, and of the edges of the KTL-sample, to quantify the coating thickness.

Measuring

Coating thickness was measured by averaging five measurements from the same image, while grain sizes were found using the linear intercept method. Both measurements were done using ImageJ.

EBSD

Electron Backscatter Diffraction (EBSD) was used to get more detailed images comparing the bulk microstructure to that of the area adjacent to the corners. Here, one KTL sample and one uncoated sample were investigated. They were cut, ground and polished as the metallography samples, but they were not cast into Epofix. They were further polished by vibrational polishing in a Buehler Vibramet 2 for about 2 h.

The samples were analysed using the EBSD detector of a Zeiss Ultra 55 LE SEM at a magnification of 200X and with a step size of 0.3 µm.

3.4.2 Tensile Testing

Three samples were tested in tension, in a Multipurpose Servohydraulic Universal Testing Machine Series LFV 100 kN, to provide an overview of the mechanical properties of the material. One sample was coated with KTL, one was anodised and one was uncoated and of the alloy with extra Ti. The resulting data were plotted as engineering stress versus engineering strain and used to determine yield stress, ultimate stress and elastic modulus for each sample. Additionally, %EL was calculated by subtracting the elastic strain from the total strain at fracture, and %AR was found by measuring the cross-section area before and after testing.

3.4.3 Surface Roughness Measurements

Surface roughness for all fatigue samples was measured using an Alicona InfiniteFocus SL. This was done to map the effects of different surface roughness between the various types of samples. The parallel area of each surface of each sample was measured, and average values of R_a, R_q, R_z, R_t and R_{max} were obtained. The highest value of R_{max} and the average value of R_a obtained for each sample was plotted against the corresponding number of cycles to fracture, and average values and standard deviations of all parameters were calculated for each sample type.

Additionally, measurements were taken of the scratch made in one of the KTL samples. Here, a heatmap indicating the height differences in and around the scratch was obtained, and waviness values were used to quantify the depth of the scratch.

3.4.4 Fatigue Testing in Air

Samples of the types uncoated, anodised, KTL, Ti uncoated and Ti anodised were all tested in fatigue in air. The samples were mainly tested at σ_a=160 or 220 MPa. The numbers of samples tested at each of these stress amplitudes for each sample type is shown in Table 3.3. Additionally, 3 uncoated samples were tested at 140 and 180 MPa, 2 at 170 MPa, and 1 at 150, 190, 200 and 210 MPa. All samples were tested in air with fully reversed cyclic loading (R=-1) and a frequency of 10 Hz. The machine was programmed to stop when a critical crack had formed, to minimise any mechanical damage that might be done to the fracture surface after critical crack formation. Fractures were completed by manual stretching of the samples.

3.4.5 Corrosion Fatigue Testing

Uncoated, anodised, Ti uncoated, Ti anodised and KTL-samples were tested in corrosion fatigue. Of the latter, 6 were scratched before testing, as described below. The numbers of samples tested at σ_a are shown in Table 3.3. All samples were first rinsed in acetone and ethanol to avoid contaminations. Next, they were mounted to an aluminium disc, such that the parallel area of the sample was just above the opening of the disc. Pattex Easy Silicone was used and given a couple of hours to harden. The disc and sample were then mounted to a plexiglass chamber, using the same silicon glue. The dimensions of the disc and chamber are shown in Figure 3.7 (a). The ready setup was allowed to harden for at least 12 h before testing.

A solution containing 5 wt% NaCl was prepared using distilled water and solid NaCl salt and transported in a plastic bottle. The sample with the chamber was fastened in the MTS 810 machine, and filled with saltwater solution from the bottle until the parallel area of the sample was covered. A sample during testing is shown in Figure 3.7 (b). All samples were tested with a frequency of 5 Hz, and conditions otherwise similar to the fatigue tests done without corrosion.

Table 3.3: Number of samples tested at each σ_a for each sample type in air and in 5 wt% NaCl.

Sample type	Nr. at 160 MPa in air	Nr. at 220 MPa in air	Nr. at 160 MPa in 5 wt% NaCl	Nr. at 220 MPa in 5 wt% NaCl
Uncoated	5	2	4	3
Anodised	3	2	4	3
KTL	3	2	3	2
KTL scratched	0	0	4	2
Ti Uncoated	3	0	3	2
Ti Anodised	3	0	3	2

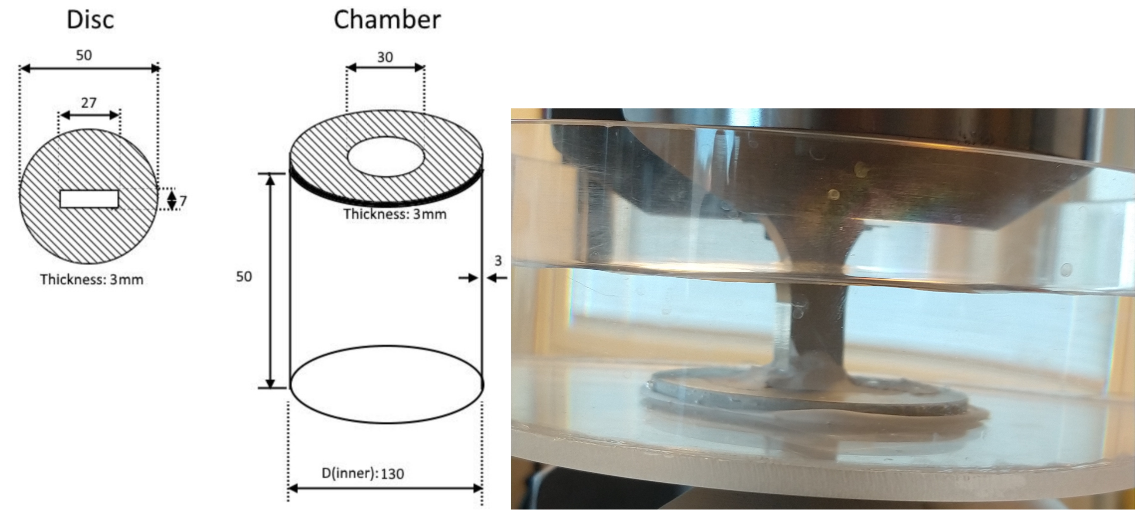

(a) (b)

Figure 3.7: (a) The dimensions of the disc and chamber used in corrosion fatigue testing, adapted from [53]. All dimensions are in mm. (b) A sample during corrosion fatigue testing.

Scratching of Samples

5 KTL-samples were scratched according to ISO 17872:2007 prior to corrosion fatigue testing. The scribe marks were made using a metallic ruler and a LEATHERMAN® Micra® pocket-knife. The ruler was placed diagonally from top to bottom corner of the sample, and scribe marks were made along the parallel area of the samples. This gave an X on each of the faces, as shown in Figure 3.8. Scratches were made before rinsing with acetone, but after surface roughness measurements. The scratch in one of the scratched samples was examined in an Alicona Infitifefocus SL, to determine the depth of the scribe mark.

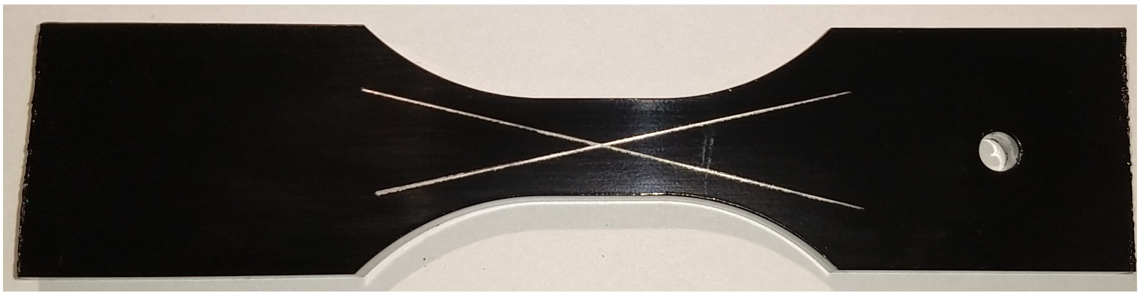

Figure 3.8: A scratched KTL sample ready for corrosion fatigue testing.

3.4.6 Corrections to R=-1

The reference data provided by SINTEF for corrosion fatigue were corrected from R=0.1 to R=-1. The least-squares method was used to approximate the coefficients for the Basquin law (b and $\sigma_f^{'}$) from the stress amplitudes and number of cycles at R=0.1. This was done for each sample type. The reduced stress amplitude (σ_{ar}) was calculated using the Smith Watson Topper equation (Equation 2.13). The number of cycles at R=-1 was then approximated by solving the Basquin law (Equation 2.14) for N_f, using the aforementioned coefficients and reduced stress amplitude.

3.4.7 Fractography

Samples representing some of the different combinations of coating, stress amplitude and corrosion exposure were examined in a Zeiss Ultra 55 LE SEM after fatigue testing. A part of approximately 1 cm height, including the fracture surface, was cut from each of the samples, to ensure maximal depth of field (see Chapter 2.9). Cutting was done using Struers Discotom-5, and the samples were rinsed in water. All samples were cleaned in an ultrasonic acetone bath for about five minutes, then rinsed with water and ethanol before insertion into the SEM. Some samples also required scrubbing, which was done with a non-metallic brush before cleaning. The samples were examined with emphasis on crack initiation and signs of corrosion. Fatigue striations were also identified for all samples, to help understand the crack propagation.

4. Results

This chapter presents the results of experiments, that were executed in order to understand the fatigue and corrosion fatigue properties, and the factors influencing them.

4.1 Tensile Tests

The results of tensile tests of one anodised sample, one KTL-coated sample and one Ti-containing uncoated sample are shown in Figure 4.1 in the form of stress-strain curves. Stress and strain axes are both engineering. The values found for E, σ_y, σ_u, %EL and %AR are shown in Table 4.1.

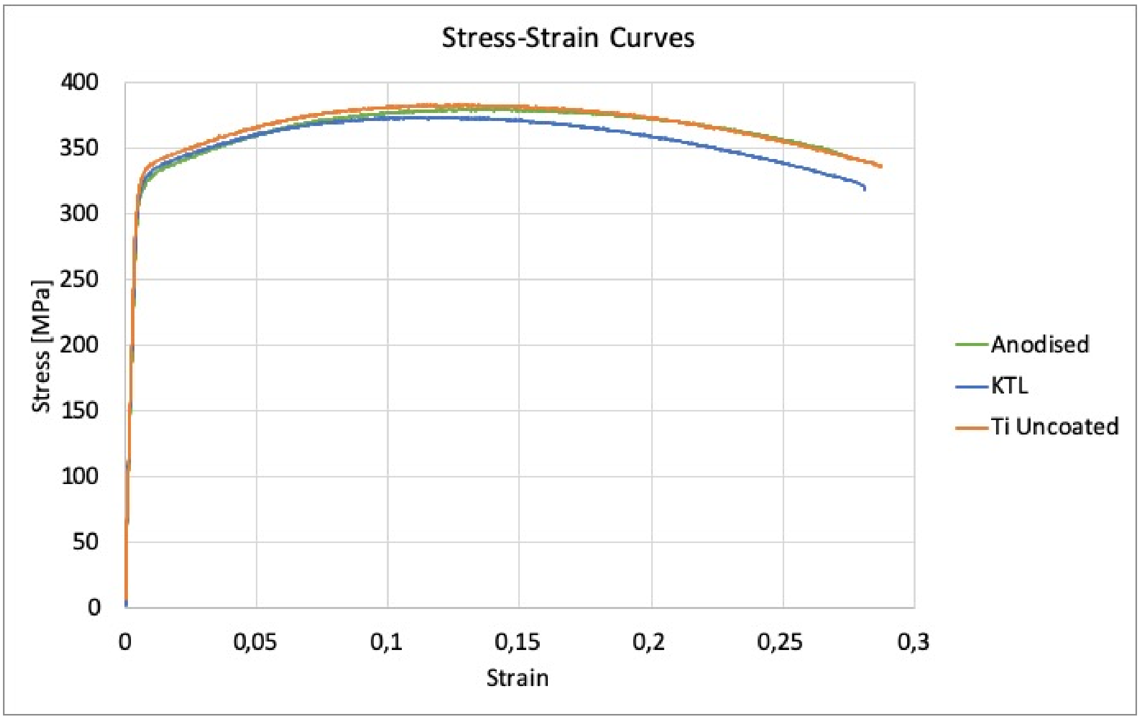

Figure 4.1: Stress-strain curves for Ti uncoated, KTL, and anodised samples.

Table 4.1: Data from tensile tests.

	E [GPa]	σ_y [MPa]	σ_u [MPa]	%EL	%AR
Anodised	69.6	320.0	379.8	26.9	28
KTL	69.5	325.0	373.9	27.6	36
Ti Uncoated	73.1	328.3	383.4	28.3	33

4.2 Metallography

Results of metallographic examinations following cutting, grinding and polishing are given in the form of images taken by light optical microscope. Figure 4.2 shows the grain structure of a KTL sample, close to the corner of the sample, while the grain structure of a Ti anodised-sample is shown in Figure 4.3. Notice the thin layer by the top edge of the former sample, where grains appear to be smaller. The results of grain size measurements in the SD are shown in Table 4.2. Figure 4.4 indicates the measured average coating thickness of the KTL layer of the first sample.

Table 4.2: Results of grain size measurements in the short transverse direction.

	Nr.	Number of Grains	Distance Covered [µm]	Grain Size [µm]
KTL	1	15	125.4	8.4
	2	21	107.6	5.1
	3	20	129.5	6.5
	avg.	18.7	120.8	6.7
Ti Anodised	1	15	101.6	6.8
	2	20	123.7	6.2
	3	22	185.4	8.4
	avg.	19.0	136.9	7.1

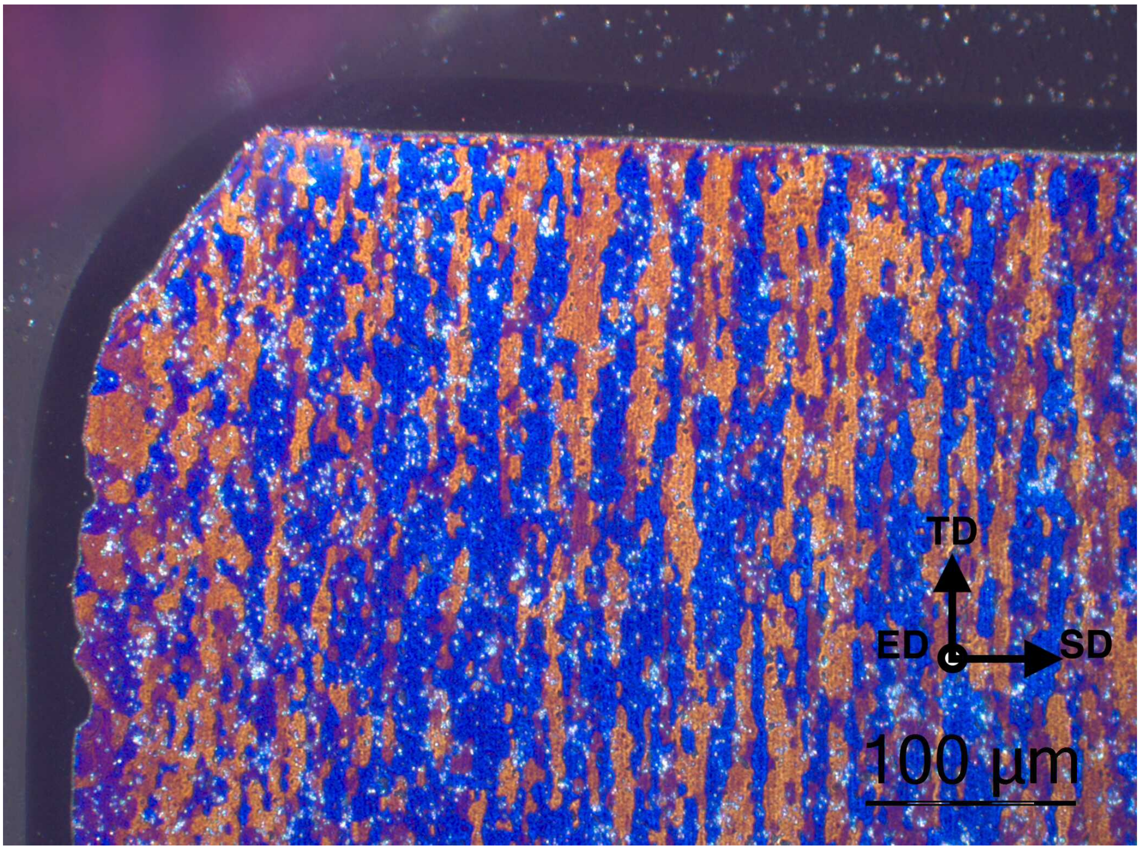

Figure 4.2: Optical micrograph of the grain structure of a KTL sample.

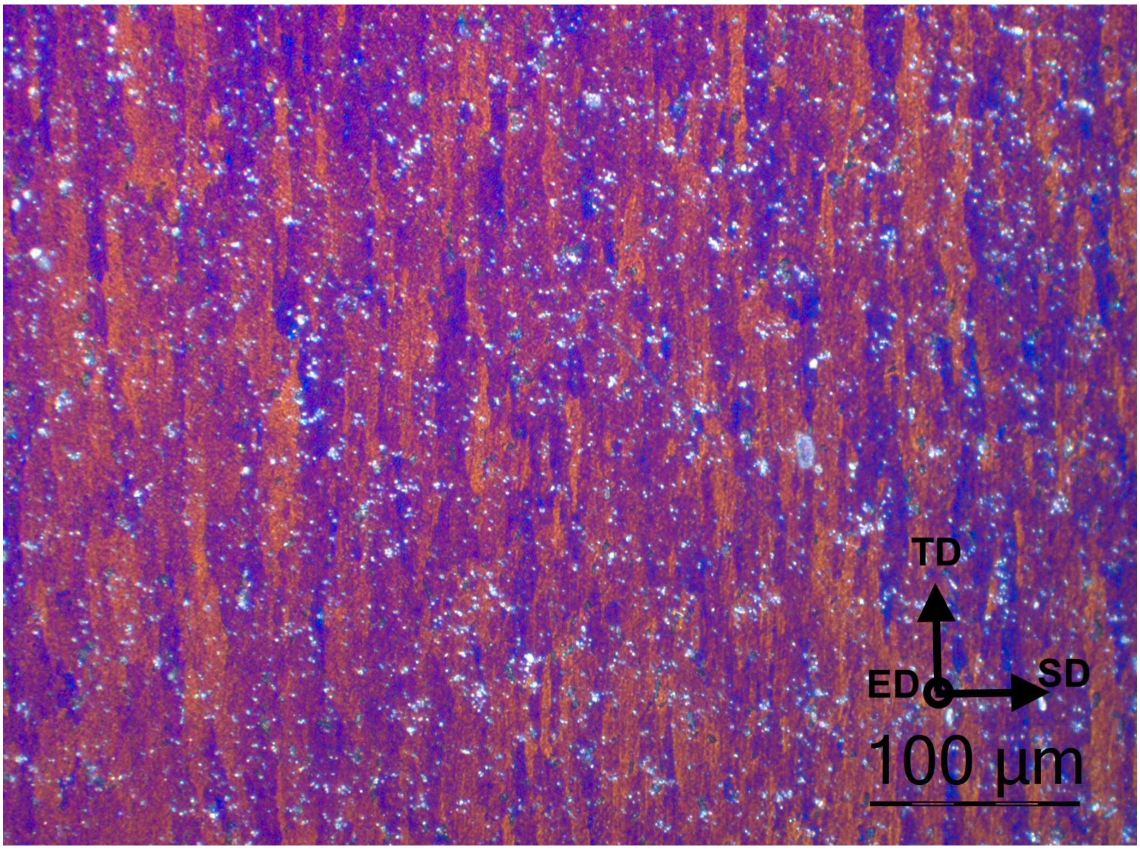

Figure 4.3: Optical micrograph of the grain structure of a Ti anodised sample.

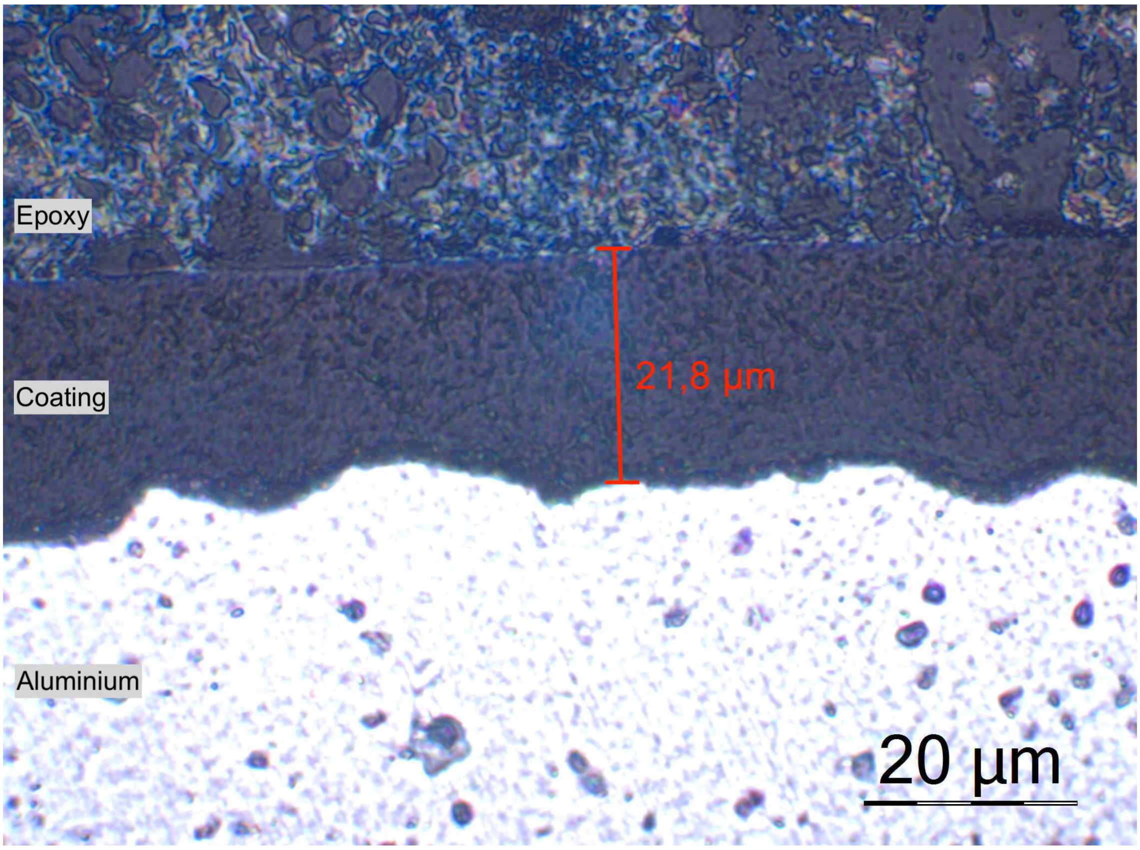

Figure 4.4: The extruded edge of a KTL sample, with measured average coating thickness.

4.3 EBSD

The results of EBSD imaging of a KTL sample and an uncoated sample are given below. The directions and meaning of the colours represented in the EBSD images are shown in Figure 4.5. Grain structures both in the centre and close to the corner of the KTL sample and the uncoated sample are shown in Figure 4.6 and Figure 4.7, respectively. Beware that there are areas of noise, especially in the former, indicating imperfect sample preparation and/or analysis.

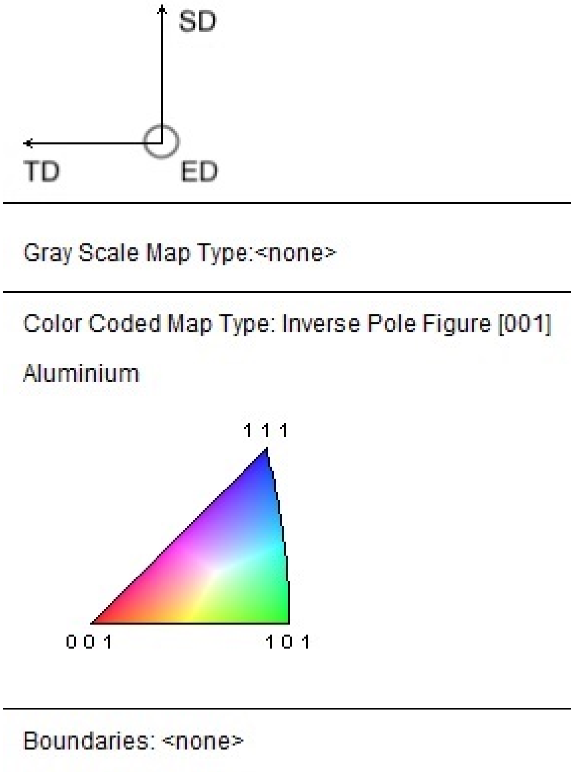

Figure 4.5: Crystallographic directions represented in EBSD images

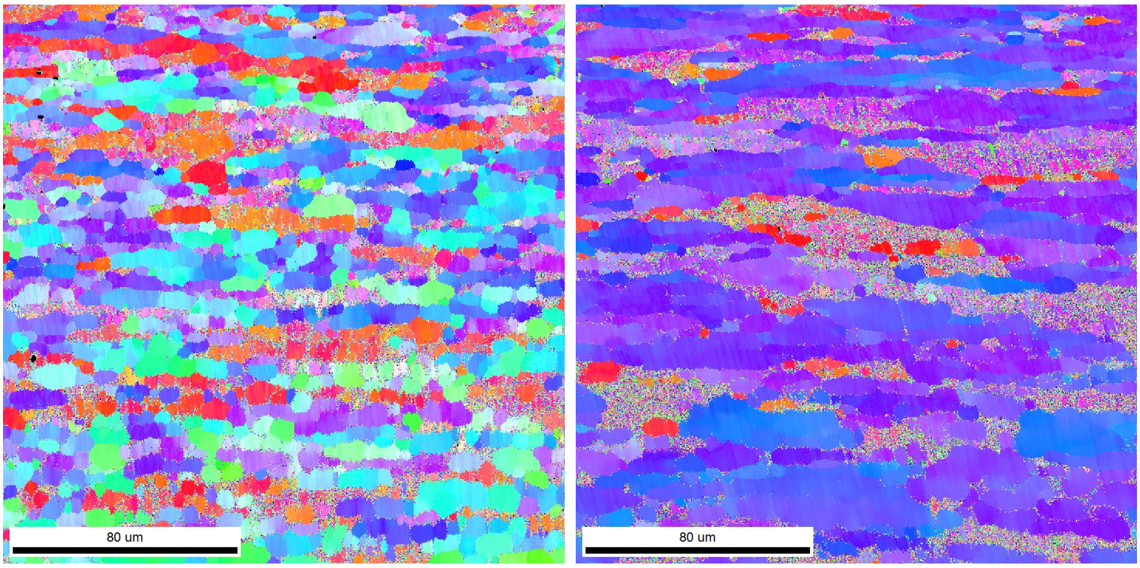

(a)

(b)

Figure 4.6: EBSD pattern from (a) a corner, and (b) the centre of a KTL sample.

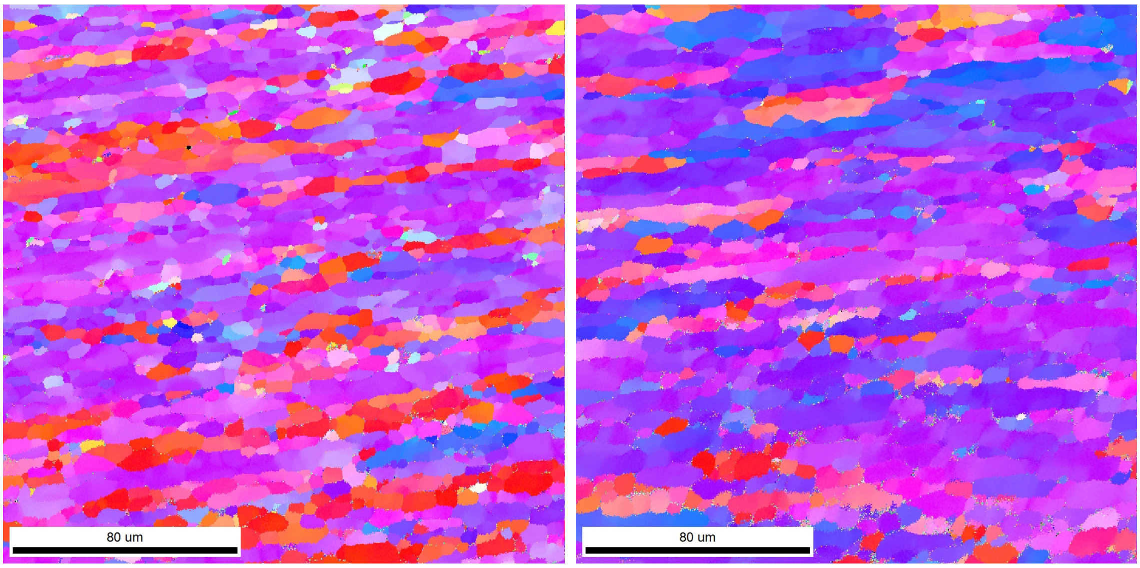

(a) (b)

Figure 4.7: EBSD pattern from (a) a corner, and (b) the centre of an uncoated sample.

4.4 Surface Measurements

Surface roughness of samples tested in air and in 5 wt% NaCl plotted against their respective numbers to failure are shown in Figures 4.8 and 4.9, respectively. The highest value of R_{max} from the 4 sides measured on each sample was used. Average values of R_a were also plotted against N_f. This is shown for samples fatigue tested in air and 5 wt% NaCl in Figures 4.10 and 4.11, respectively. Mean and standard deviation (STD) of surface roughness values for the different sample types are given in Table 4.3. A complete table of surface roughness values from all 4 sides of each fatigue sample is given in Appendix A. Measurements of one of the scratches in a scratched KTL-sample is shown in Figure 4.12. The measured values for waviness in this area are given in Table 4.4.

Table 4.3: Mean and standard deviation values of surface roughness for the different sample types.

	KTL	Uncoated	Anodised	Ti Uncoated	Ti Anodised
Mean Ra [µm]	0.602	0.764	1.367	0.745	1.209
STD Ra [µm]	0.068	0.160	0.179	0.189	0.223
Mean Rq [µm]	0.765	0.977	1.723	0.953	1.550
STD Rq [µm]	0.091	0.212	0.221	0.251	0.312
Mean Rt [µm]	5.709	6.877	11.625	6.953	11.354
STD Rt [µm]	1.242	1.873	1.968	1.977	3.220
Mean Rz [µm]	4.419	5.373	9.388	5.222	8.774
STD Rz [µm]	0.646	1.255	1.167	1.302	1.728
Mean Rmax [µm]	5.371	6.575	11.006	6.524	11.028
STD Rmax [µm]	1.148	1.823	1.899	1.731	3.298

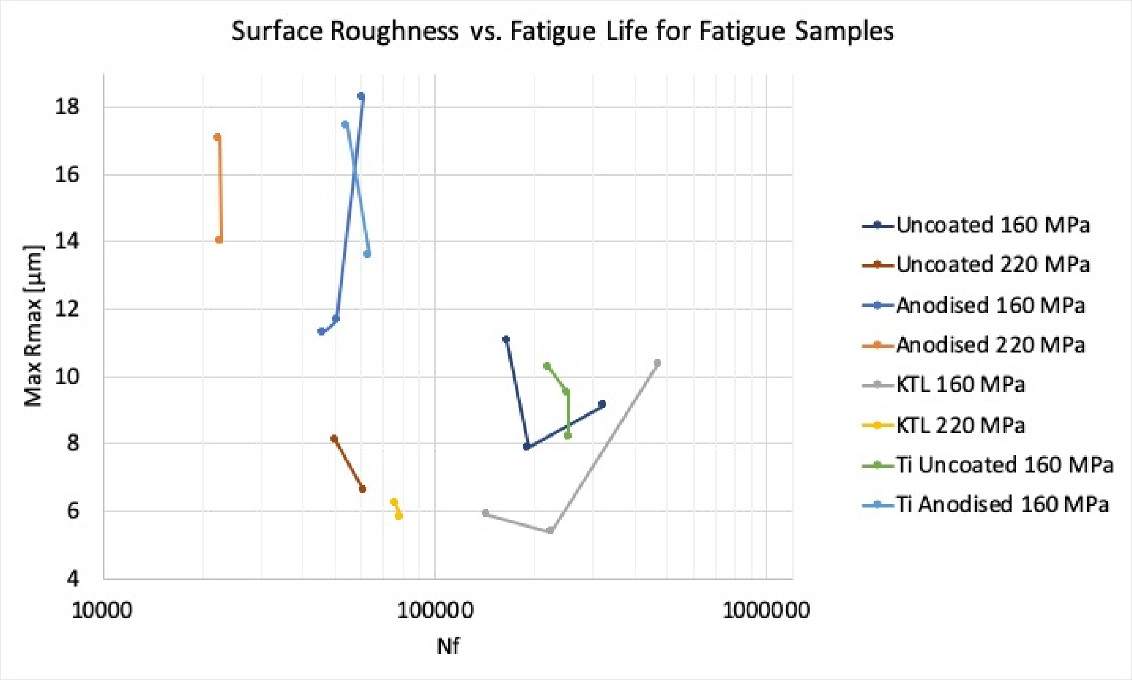

Figure 4.8: Maximum values of R_{max} plotted against N_f for samples tested in air.

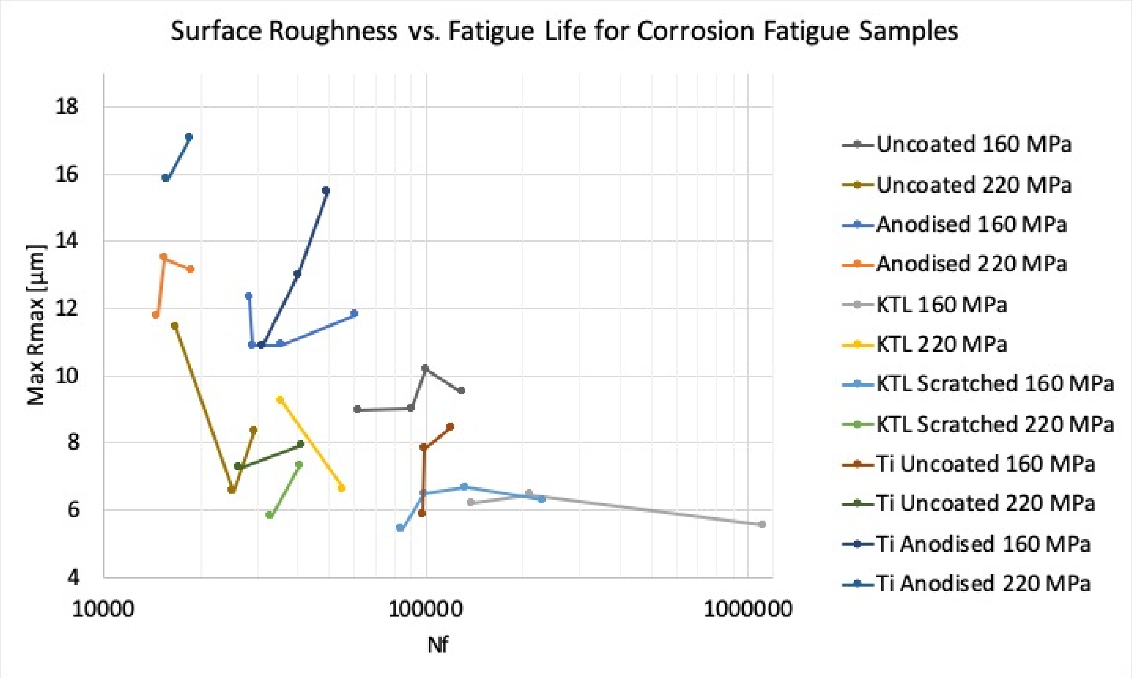

Figure 4.9: Maximum values of R_{max} plotted against N_f for samples tested in 5 wt% NaCl.

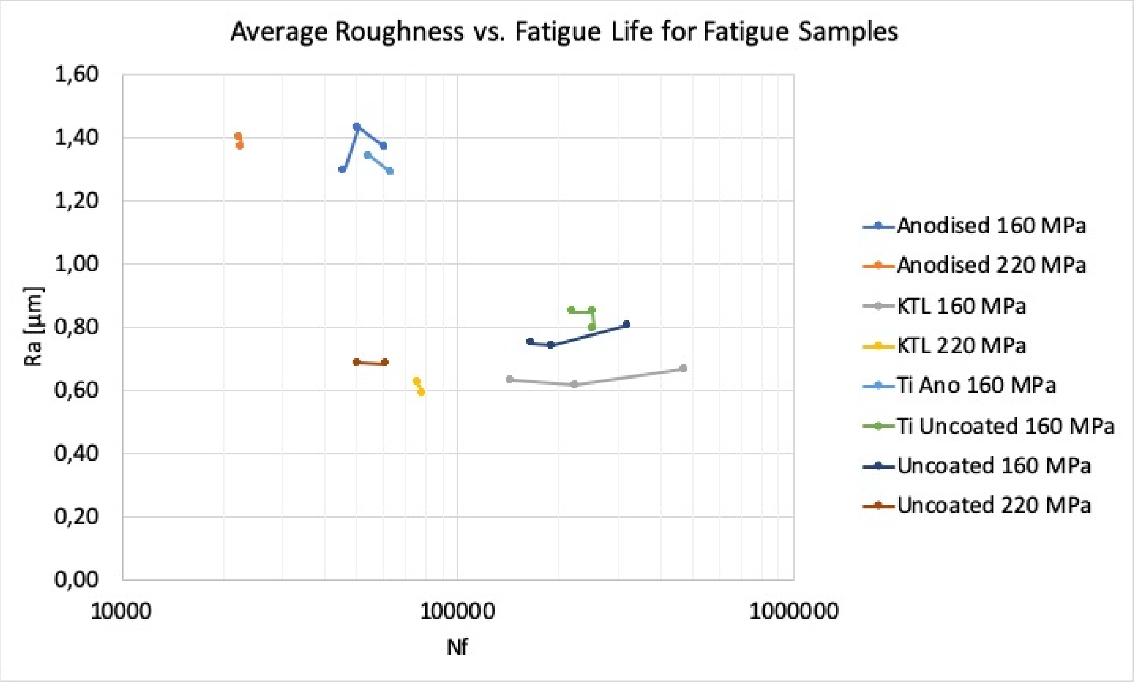

Figure 4.10: R_a vs N_f for samples fatigue tested in air.

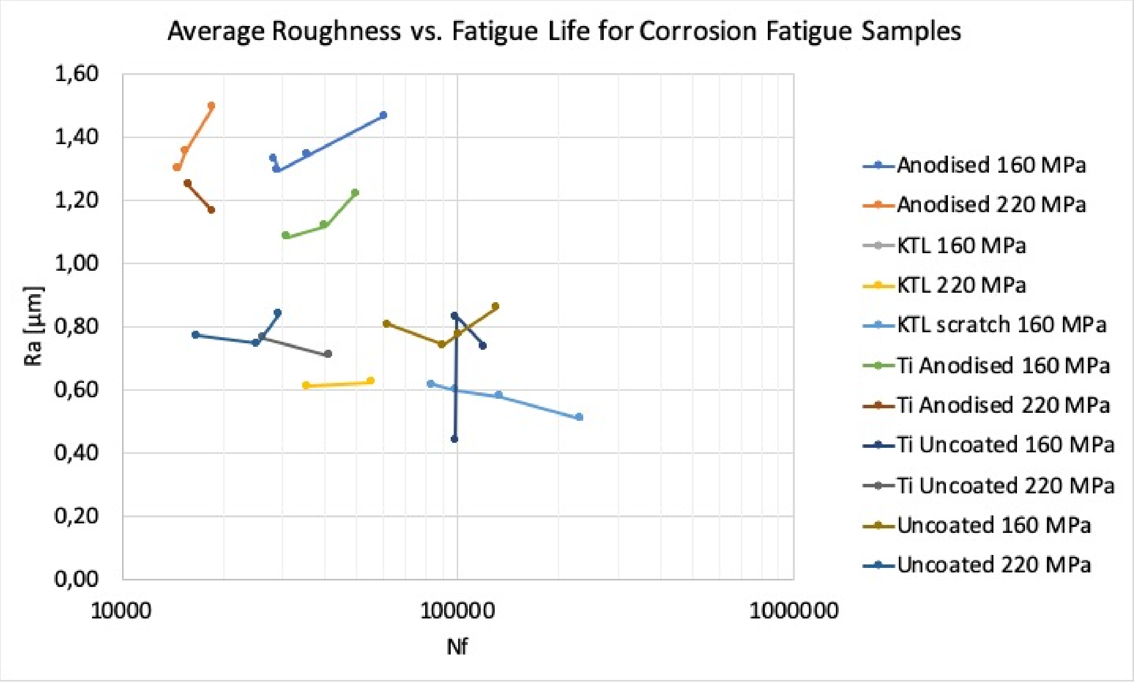

Figure 4.11: R_a vs N_f for samples fatigue tested in 5 wt% NaCl.

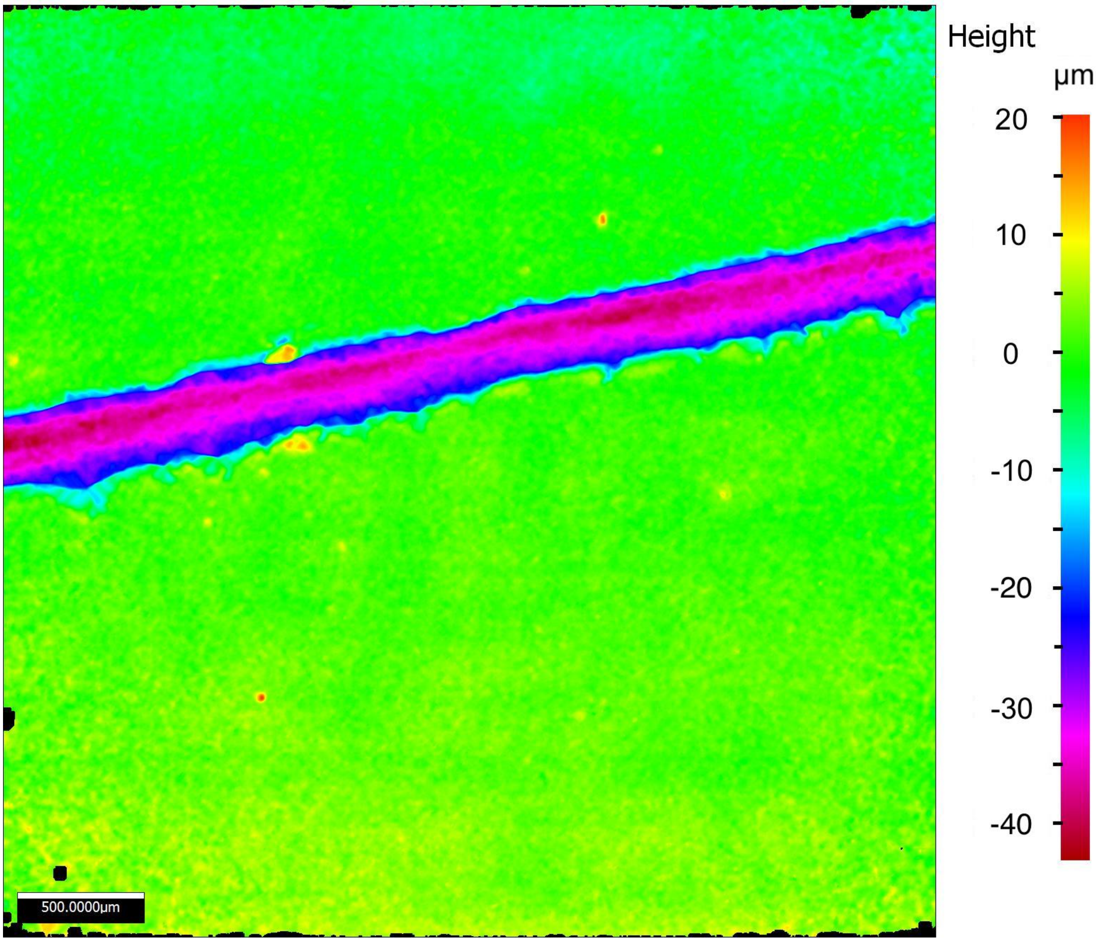

Figure 4.12: Heat map indicating height differences in a scratched KTL sample.

Table 4.4: Waviness values for the scratched sample, in the area shown in Figure 4.12.

Name	Value [µm]	Description
W_a	9.50	Average waviness of profile
W_q	11.80	Root-Mean-Square waviness of profile
W_t	33.92	Maximum peak to valley height of waviness profile
W_z	13.32	Mean peak to valley height of waviness profile
W_{max}	32.16	Maximum peak to valley height of waviness profile within a sampling length

4.5 Fatigue and Corrosion Fatigue

Results from fatigue tests done in air and in 5 wt% NaCl are shown by S-N curves in Figures 4.13 and 4.14, respectively. Arrows next to points indicate that they were stopped without fracture, having exceeded the run-out limit at 10^6 cycles. Note that some series were tested at only one stress amplitude. These are not represented by a line, only by the individual points. The reference S-N curve provided by SINTEF (Figure 3.4) was corrected from R=0.1 to R=-1 through SWT (Equation 2.13) and the Basquin law (Equation 2.14). The resulting S-N curve is shown in Figure 4.15.

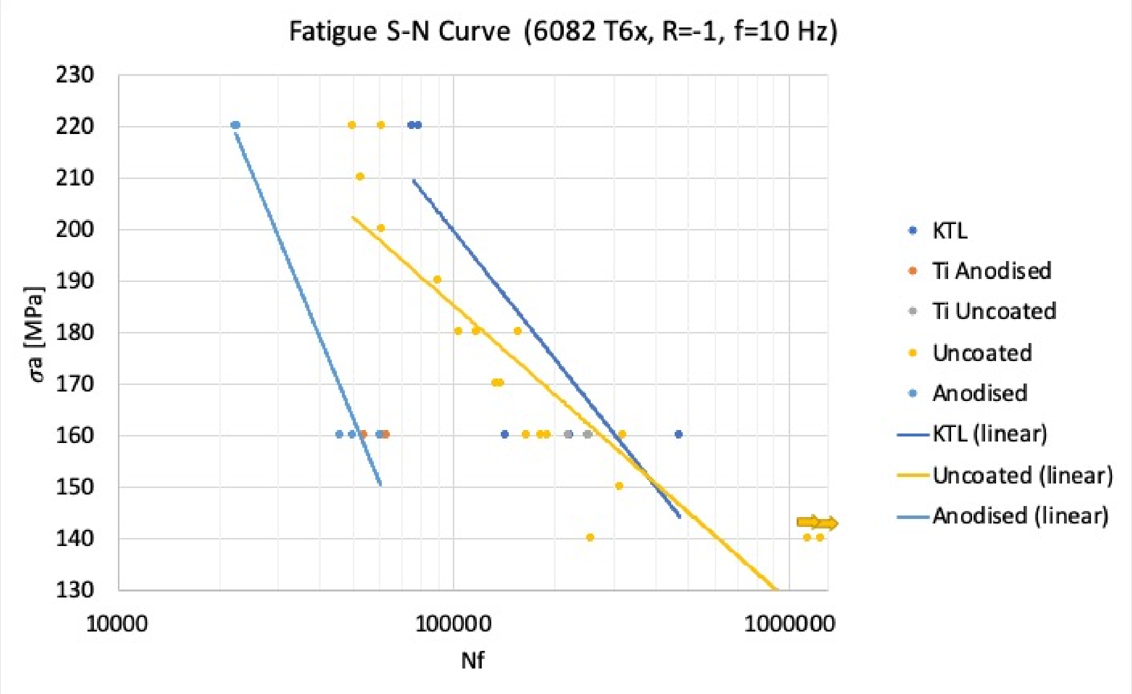

Figure 4.13: S-N curve of samples tested in air.

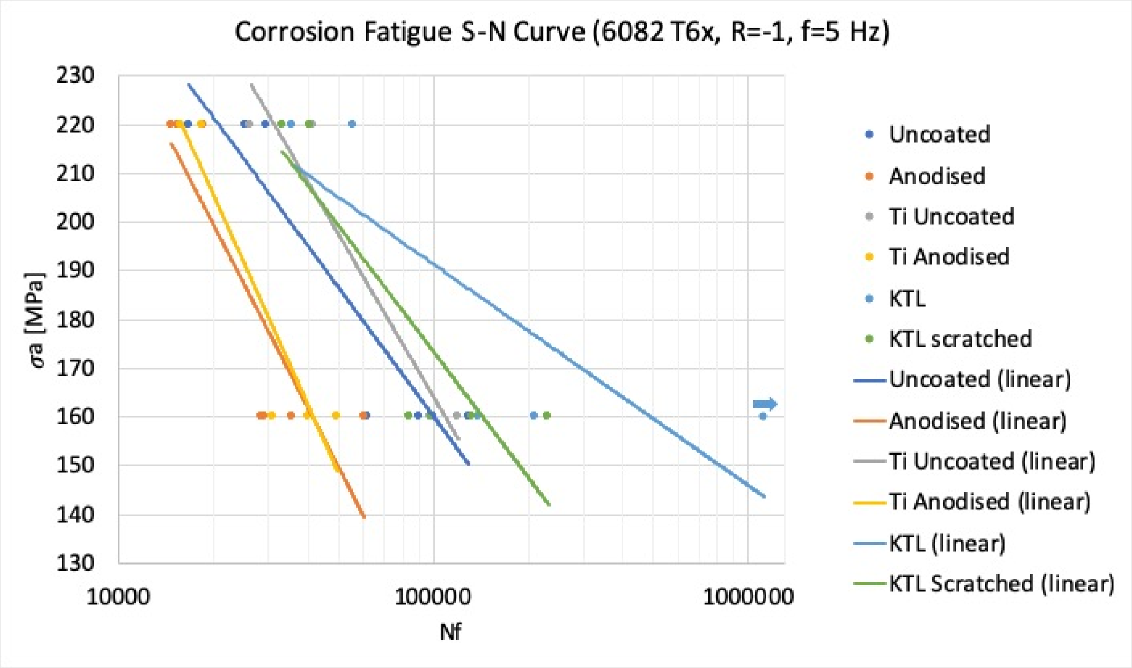

Figure 4.14: S-N curve of samples tested in 5 wt% NaCl.

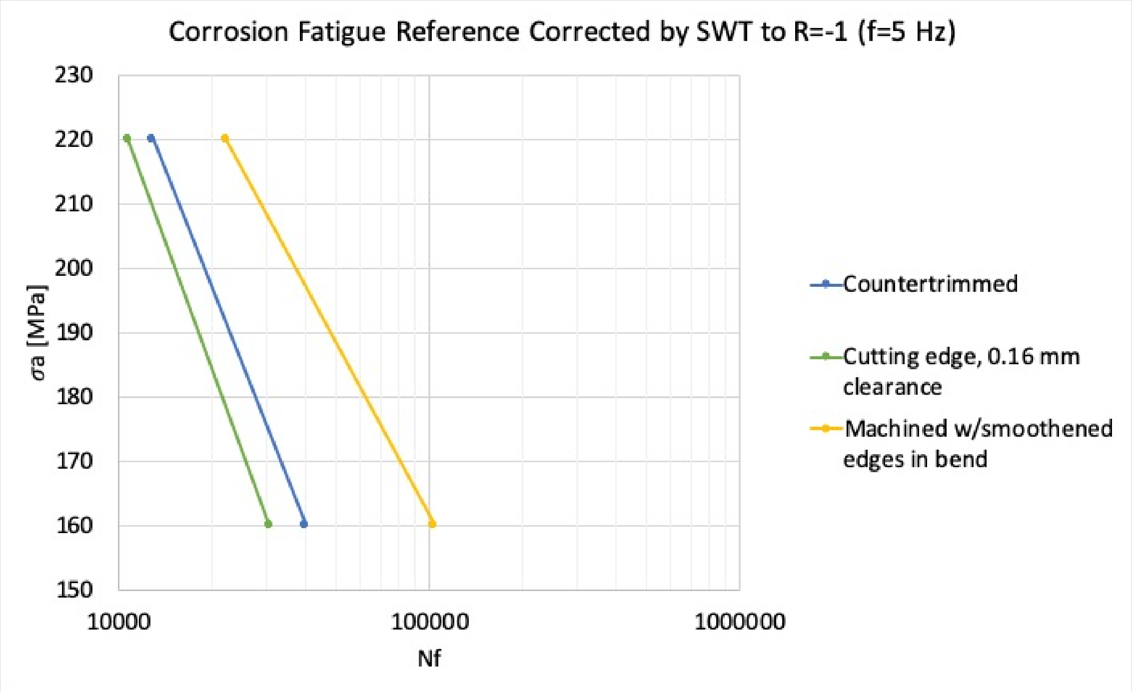

Figure 4.15: S-N curve of reference data from SINTEF, tested at R=0.1 in 5 wt% NaCl, corrected to R=-1.

4.6 Fracture Characterisation

The results of fracture surface investigations are given through SEM micrographs below, for samples fatigue tested in air and in 5 wt% NaCl. The number of cycles to fracture is given for each sample, along with the corresponding stress amplitude.

4.6.1 Samples Fatigue Tested in Air

One KTL, one Ti anodised and one Ti uncoated sample were investigated. The fracture surfaces were characterised through crack initiation sites, ridge marks and fatigue striations.

KTL, σ_a=160 MPa, N_f=143 990

The full fracture of the KTL sample is shown in Figure 4.16 (a), with indications of the areas where fatigue and overload failure were found to have occurred. Figure 4.16 (b) shows fatigue striations. These are perpendicular to the top right corner of the sample, and the fracture initiation point shown in Figure 4.16 (c) and (d). The arrows in (c) indicate the crack propagation direction.

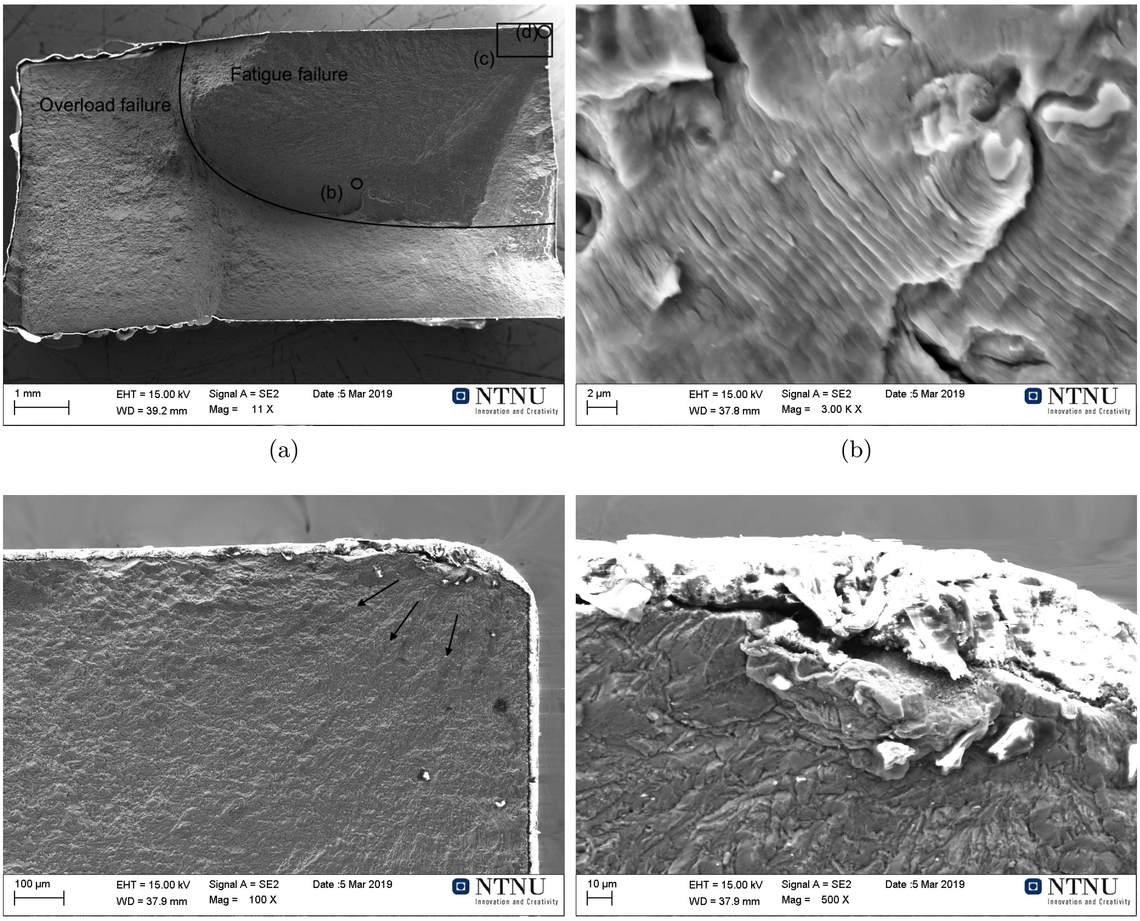

(a) (b) (c) (d)

Figure 4.16: SEM images of a KTL-sample fatigue tested in air. (a) Full fracture surface, with indication of the areas magnified in (b), (c) and (d). (b) Fatigue striations. (c) Apparent crack propagation direction from the fracture initiation site. (d) Fracture initiation site.

Ti Uncoated, σ_a=160 MPa, N_f=251 575

The Ti uncoated sample is presented in the same way, with the full fracture surface, fatigue striations, crack propagation direction and crack initiation site shown in Figure 4.17 (a), (b), (c) and (d), respectively.

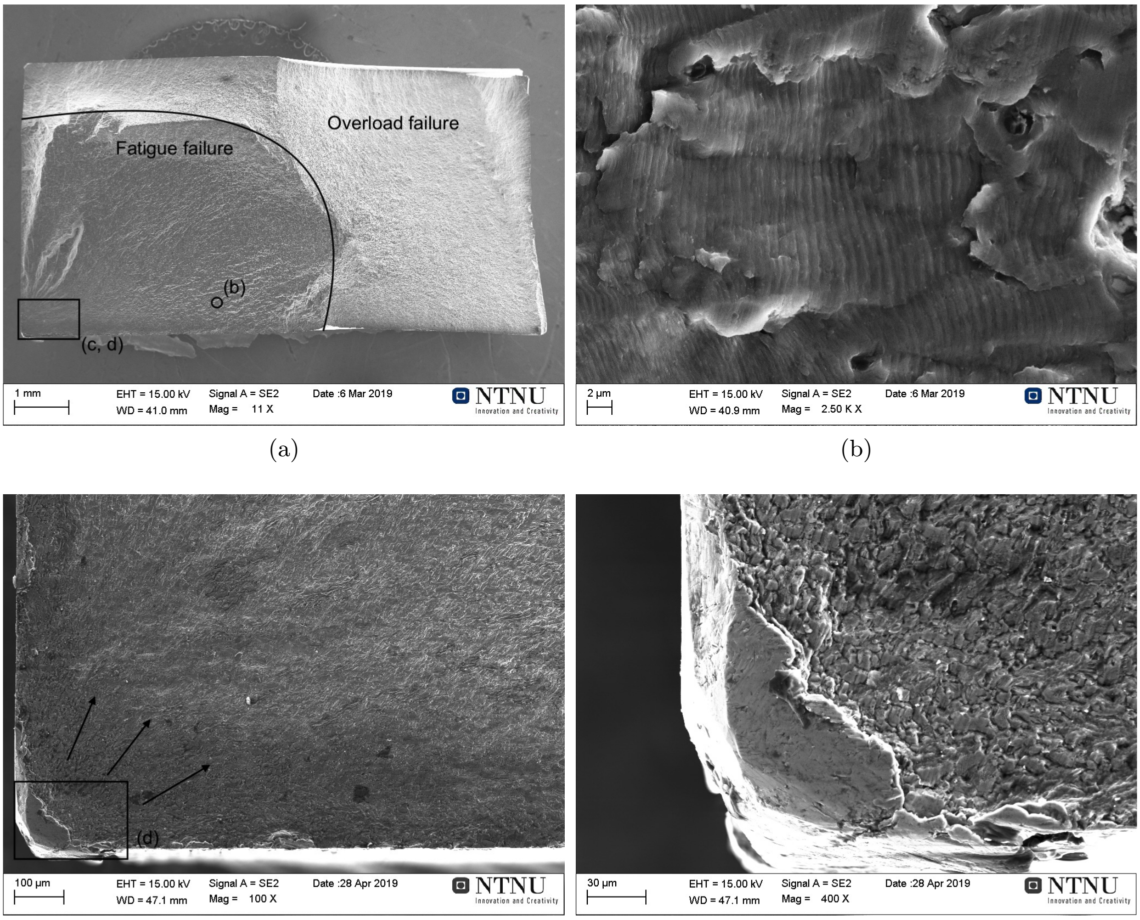

(a) (b)

(c) (d)

Figure 4.17: SEM images of a Ti uncoated sample fatigue tested in air. (a) Full fracture surface, with indication of the areas magnified in (b), (c) and (d). (b) Fatigue striations. (c) Crack initiation site, with apparent crack propagation direction. (d) Higher magnification of the crack initiation site.

Ti Anodised, σ_a=160 MPa, N_f=63 284

In the Ti anodised sample, several initiation sites were found, as indicated in Figure 4.18 (a). Two of these are shown in Figure 4.18 (b) and (c), and the direction on the striations shown in Figure 4.18 (d) indicate crack propagation from one of the closest initiation sites. Notice the direction of the ridge marks by the edges in (b) and (c), all more or less parallel to each other.

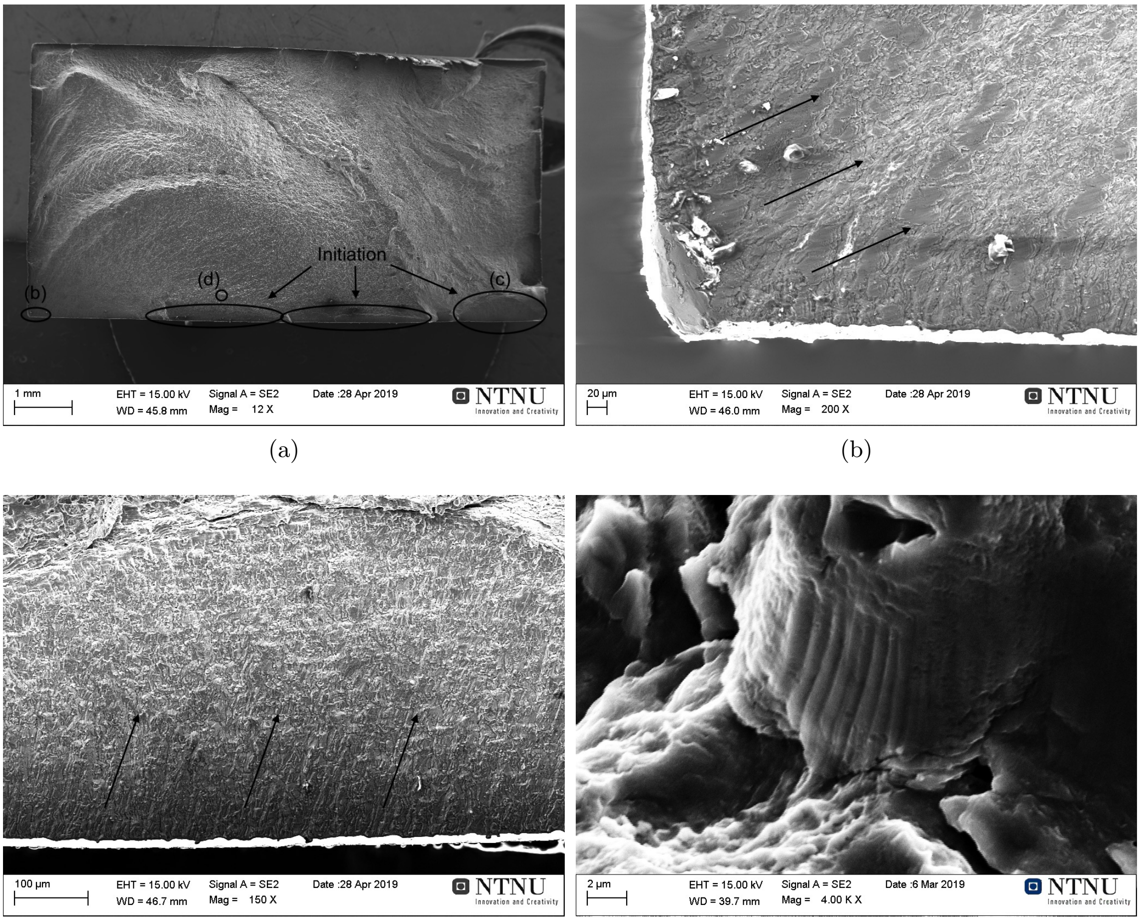

(a) (b)

(c) (d)

Figure 4.18: SEM images of a Ti anodised sample fatigue tested in air. (a) Full fracture surface, with indication of the areas magnified in (b), (c) and (d). (b) Crack initiation site, with apparent crack propagation direction. (c) A less critical fatigue crack. (d) Fatigue striations.

4.6.2 Corrosion Fatigue Samples

Of the samples fatigued in 5 wt% NaCl, fracture surfaces from two uncoated, one anodised, one Ti anodised, one KTL and one KTL scratched samples are presented. Signs of corrosion are highlighted where they were found.

Uncoated, σ_a=160 MPa, N$_f$=61 922

The full fracture surface of the first uncoated sample is shown in Figure 4.19 (a), with indications of the areas where fatigue and overload failure occurred. Figure 4.19 (b) shows striations from the fatigue area, while (c) shows dimples from the overload failure area. Figure 4.19 (d) shows a pattern reminiscent of the grain structures shown in Figures 4.2 and 4.3.

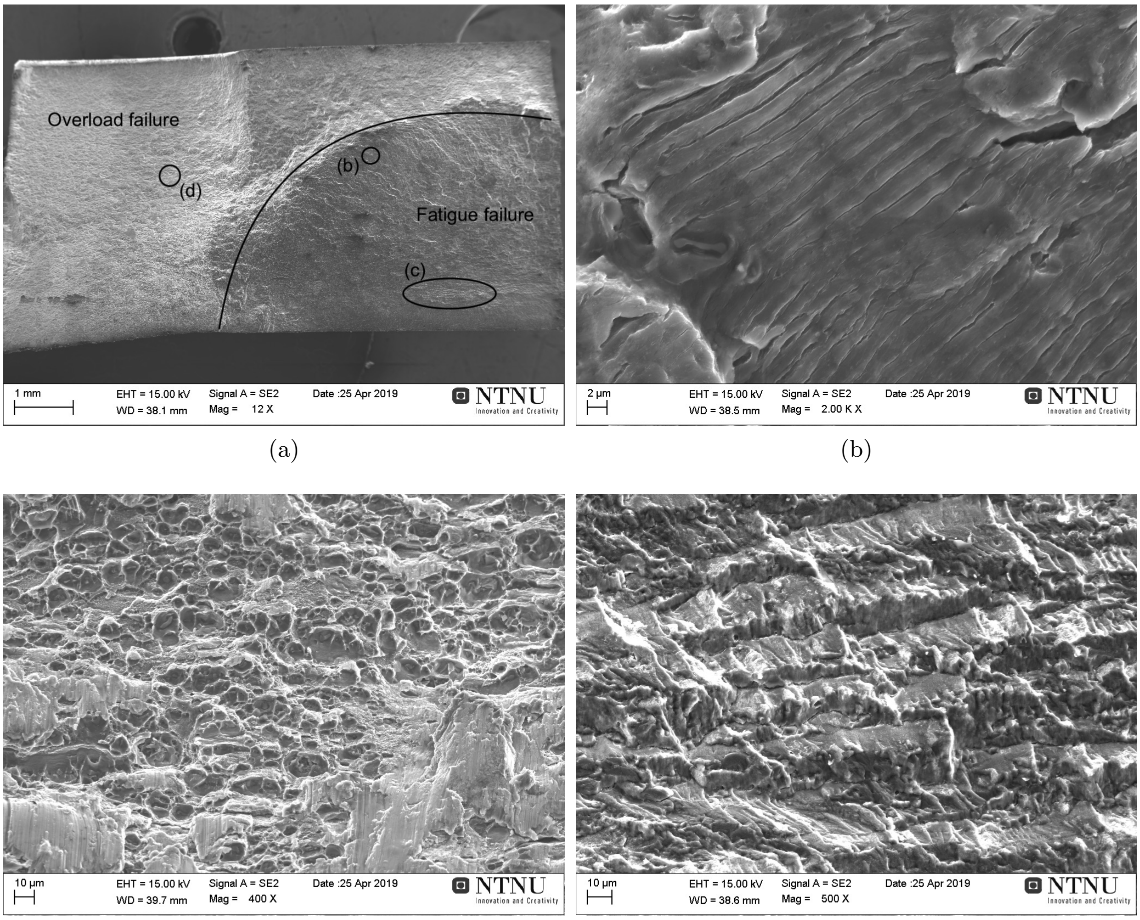

(a) (b)

(c) (d)

Figure 4.19: SEM images of an uncoated sample fatigue tested in 5 wt% NaCl. (a) Full fracture surface, with indication of the magnified shown in (b), (c) and (d). (b) Fatigue striations. (c) Dimples characteristic of ductile fractures. (d) Grain structure-like pattern.

Uncoated, σ_a=160 MPa, N_f=129 918

The full fracture surface of the second uncoated sample is shown in Figure 4.20 (a). In Figure 4.20 (b), the area adjacent to the crack initiation site is shown, with arrows indicating the apparent crack propagation directions. Figure 4.20 (c) shows a crack initiation site. Note that a similar damage was found right next to it. Fatigue striations are shown in Figure 4.20 (d).

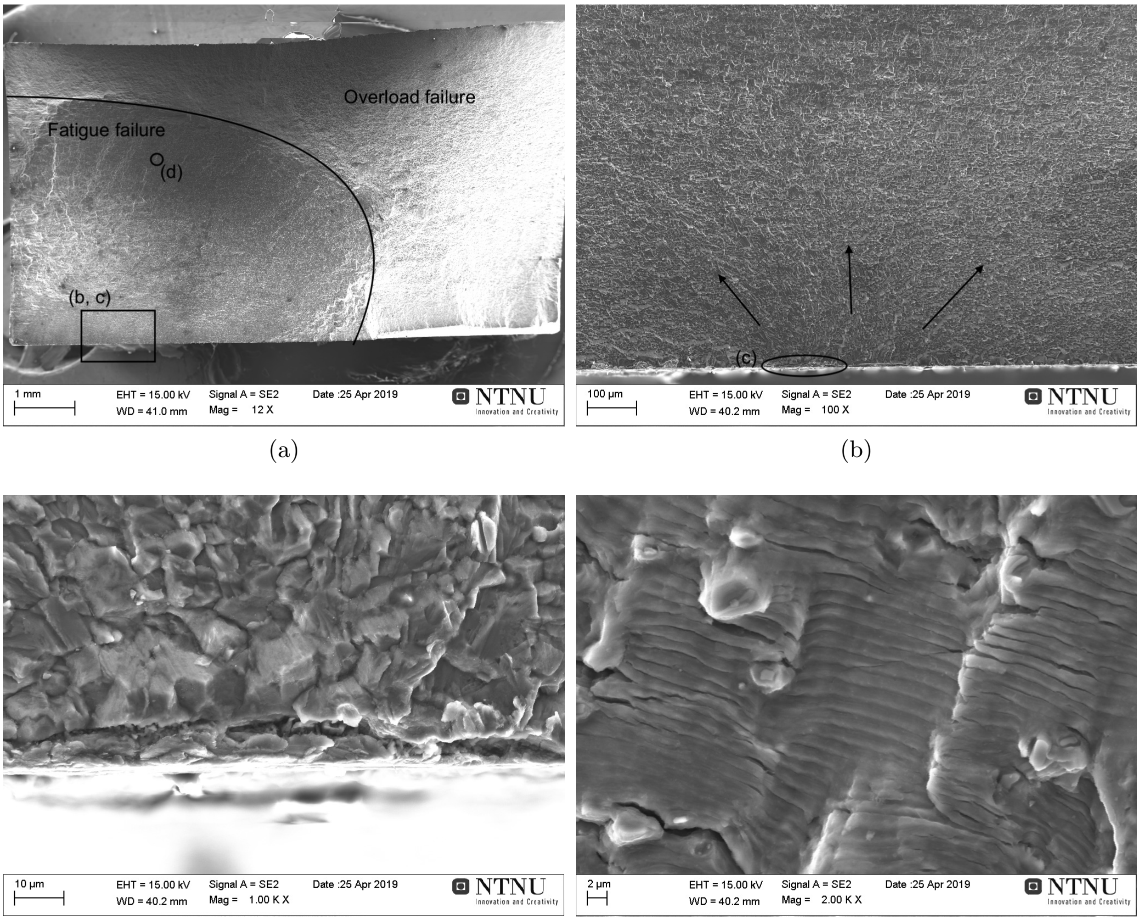

(a) (b)

(c) (d)

Figure 4.20: SEM images of an uncoated sample fatigue tested in 5 wt% NaCl. (a) Full fracture surface, with indication of the areas magnified in (b), (c) and (d). (b) Area adjacent to the fracture initiation site. (c) Fracture initiation site. (d) Fatigue striations.

Anodised, σ_a=160 MPa, N$_f$=29 007

The fatigue failure area of the anodised sample is shown in Figure 4.21 (a). No clear initiation site was found for this sample, but the ridge marks indicate a crack initiation in the area circled in the Figure. The striations in Figure 4.21 (b) are oriented approximately perpendicularly to this area.

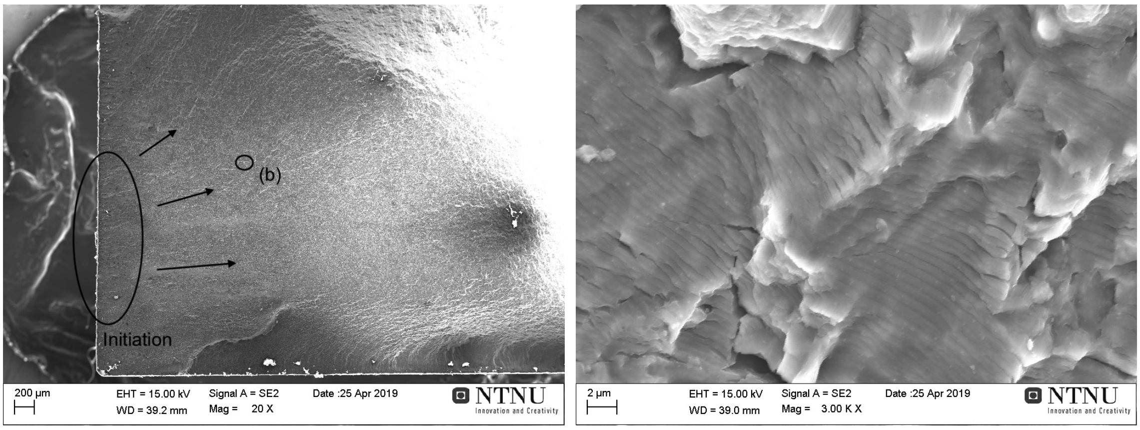

(a) (b)

Figure 4.21: SEM images of an anodised sample fatigue tested in 5 wt% NaCl. (a) Fatigue fracture area and critical crack initiation site, with indication of the area magnified in (b). (b) Fatigue striations.

KTL Scratched, σ_a=220 MPa, N$_f$=40 615

The fatigue failure area of the scratched KTL sample is shown in Figure 4.22 (a). The fatigue striations in (b) are oriented approximately normal to the fracture initiation site shown in (c). Another fracture initiation site was found in the area shown in Figure 4.22 (d), which is close to one of the scratches. Arrows indicate apparent crack propagation direction. Fatigue striations from this area are shown in Figure 4.22 (e), and appear to be oriented normal to the fracture initiation site in (f).

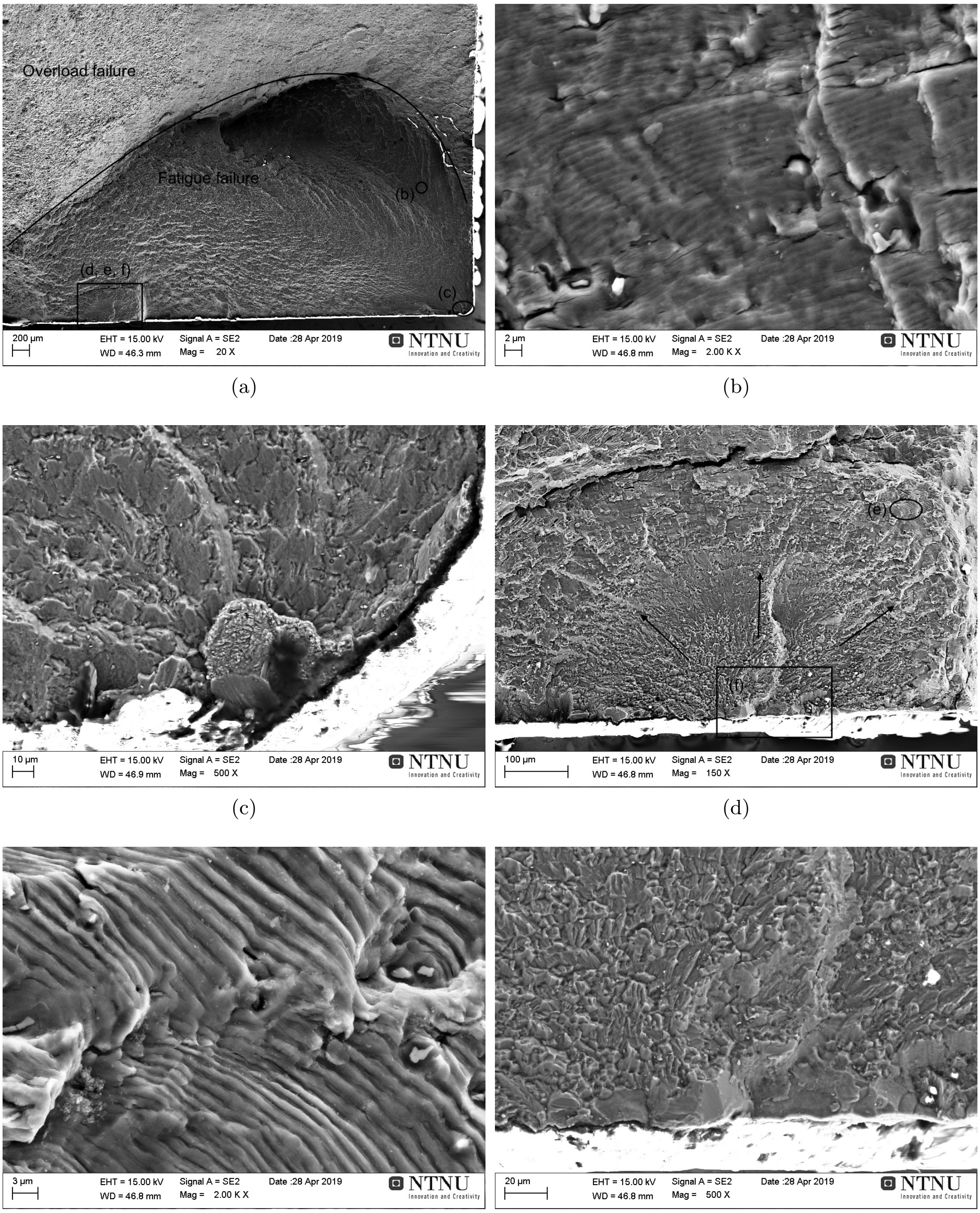

(a) (b)

(c) (d)

(e) (f)

Figure 4.22: SEM images of a KTL scratched sample fatigue tested in 5 wt% NaCl. (a) Fatigue fracture area, with indication of the areas magnified in (b), (c), (d), (e) and (f). (b) Fatigue striations. (c) Crack initiation site. (d) Area with another crack initiation site, close to the scratch. (e) Fatigue striations close to the second initiation site. (f) High magnification of the second crack initiation site.

Ti Anodised, σ_a=160 MPa, N$_f$=31 054

The fatigue failure area of the Ti anodised sample is shown in Figure 4.23 (a). The fatigue striations shown in Figure 4.23 (b) are approximately perpendicular to the crack initiation site in the corner shown in (c). However, the apparent crack propagation direction indicated in Figure 4.23 (d) indicates a critical crack initiated from the edge.

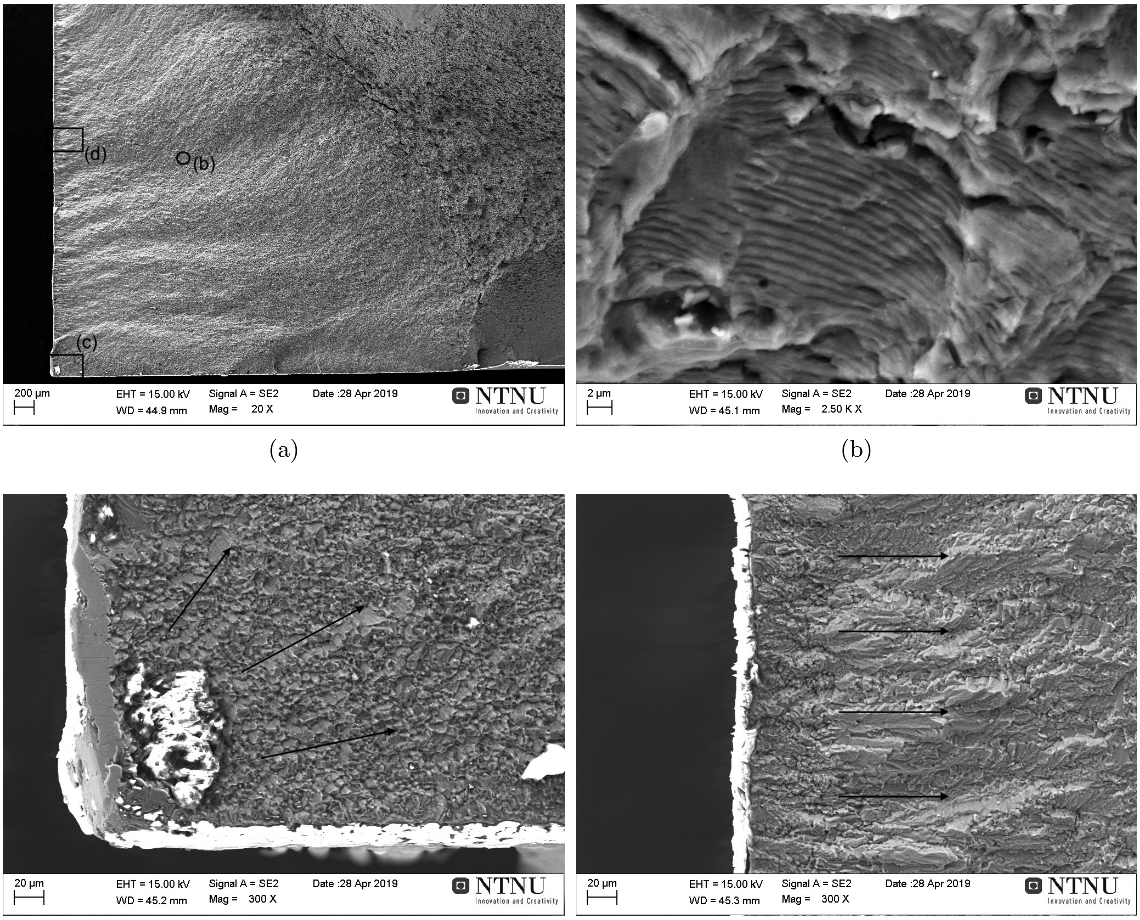

(a) (b)

(c) (d)

Figure 4.23: SEM images of a Ti anodised sample fatigue tested in 5 wt% NaCl. (a) Fatigue failure area, with indication of the areas magnified in (b), (c) and (d). (b) Fatigue Striations. (c) Crack initiation site, with indications of apparent crack propagation direction. (d) Indication of apparent crack propagation direction close to an edge.

KTL, σ_a=160 MPa, N$_f$=139 926

The complete fracture surface of the KTL sample is shown in Figure 4.24 (a), with an indication of the areas where fatigue and overload failure have occurred. The area with fatigue is magnified in Figure 4.24 (b). Notice the direction of the ridge marks towards the corner, where a crack initiation site is indicated in Figure 4.24 (c). The fatigue striations in Figure 4.24 (d) appear to be oriented perpendicularly to this site.

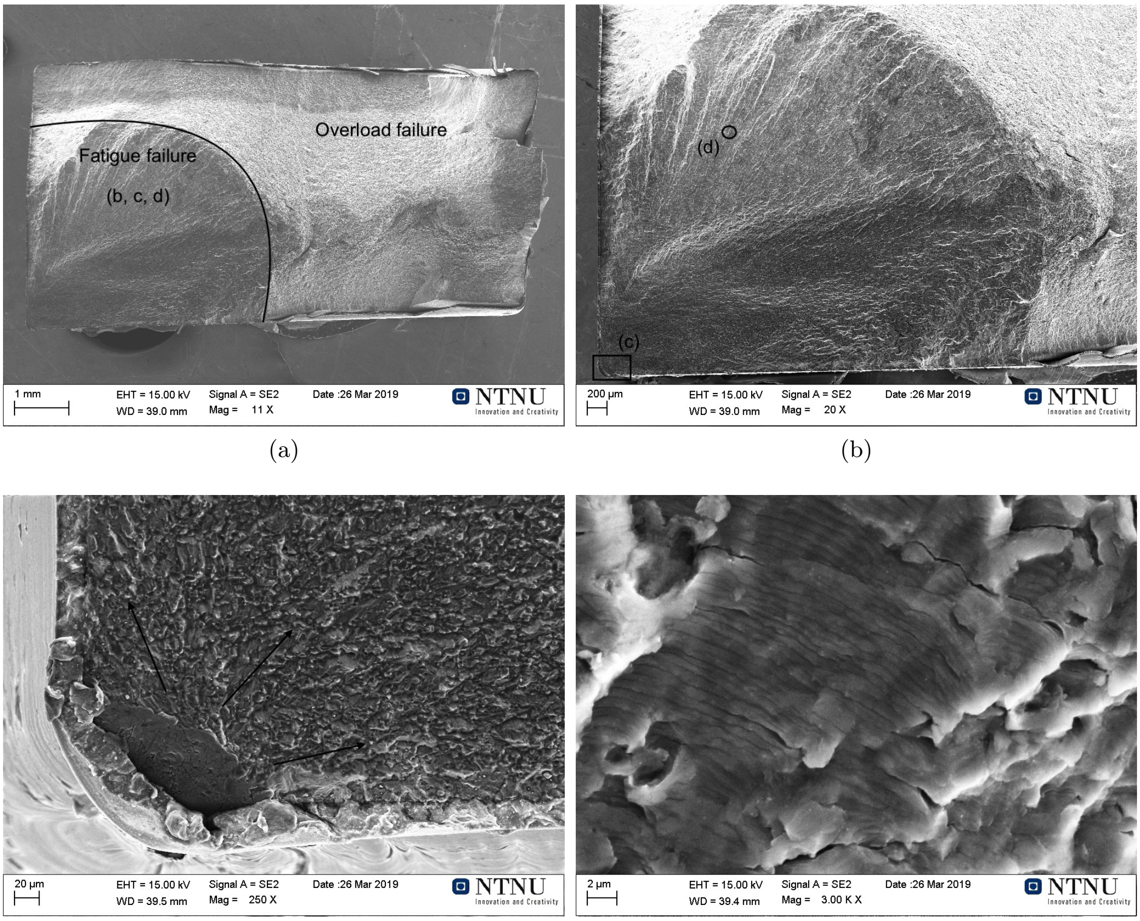

(a) (b)

(c) (d)

Figure 4.24: SEM images of a KTL sample fatigue tested in 5 wt% NaCl. (a) Full fracture surface, with indication of the areas where fatigue and overload failure have occurred. (b) Fatigue failure area, with indication of the areas magnified in (c) and (d). (c) Critical crack initiation site, where apparent crack propagation direction is indicated. (d) Fatigue striations.

5. Discussion

The results of experimental investigations are discussed and compared to theory and reference data below, and considered in terms of applicability to the full-scale component made by Benteler.

5.1 Mechanical Properties and Microstructures

The results of grain size measurements in the short transverse direction of one KTL and one Ti anodised sample were shown in Table 4.2. The average sizes found were 6.7 and 7.1 µm, respectively. These tiny grains imply a material suitable for fatigue applications, as crack initiation in aluminium is known to be aided by the formation of persistent slip bands, which are less influential in smaller grains. Note that the counting of grains in lamellar microstructures such as the ones shown in Figures 4.2 and 4.3 is an inaccurate process. Therefore, it is sufficient to say that the grain size was roughly 7 µm for both samples. In the previous work, it was established that anodising did not affect the grain structure, and the sizes regiven in Table 3.2 are both roughly equal to those found here. Therefore, it is concluded that grain size was not affected either by coating with KTL, alloying with Ti or by the combination of alloying with Ti and anodising. A reported effect of alloying with Ti was grain refinement (see Chapter 2.2.1), but no such effect was seen here. However, it could be that the extra Ti impedes recrystallisation. As no recrystallisation was observed for the uncoated or anodised samples either with or without extra Ti, any such effect would not be discovered in this work.

For the KTL sample, signs of recrystallisation was identified. Notice the change in its grain structure towards the corner and the upper edge in Figure 4.2. This was also shown by the EBSD analysis, as seen in Figure 4.6. The material appears to have recrystallised close to the edge, which is not desirable. Recall that the samples received a drying treatment during the coating process, at 160 °C for 20 min. Also, because few details were provided regarding the coating process, it is perceivable that some other pretreatments were included, that may be responsible for the observed recrystallisation. It is probable that the samples recrystallised in the surface layer at some time during the coating process. The recrystallised layer is really thin, at most the size scale of a single grain in the short transverse direction. It would not be expected, therefore, that this recrystallisation should affect the fatigue properties. Still, it should be seen as an indication that higher temperature and/or longer time could lead to significant recrystallisation.

The results of tensile tests are shown in the form of stress-strain curves in Figure 4.1, and as mechanical properties in Table 4.1. These results indicate slight differences between the anodised, the KTL, and the Ti uncoated samples. The Young's modulus (E) ranges from 69.5 and 69.6 in the KTL and anodised samples respectively, to 73.1 GPa in the Ti uncoated sample. As seen in the theory in Table 2.4 and the results from previous work in Table 3.2, Young's modulus of 69-70 GPa is expected. The observed increase from this in the Ti uncoated sample may be connected to the alloying changes. However, the increase in Ti is only from 0,01 to 0,09 wt% (as shown in Table 3.1), thus the difference in E is surprisingly large. At this point, it must be noted that the strain values used to calculate Young's modulus in particular are very low, and some inaccuracy must be expected.

The differences observed for yield stress, ultimate stress and elongation are all more as expected. Surface changes for KTL and anodised samples, along with alloy changes for the Ti uncoated, and possibly microstructural changes for the KTL sample, are all expected to influence these properties. The anodised sample showed lower yield stress (σ_y=320.0 MPa, compared to 328.3 MPa for the Ti uncoated sample), which could be connected to its brittle surface. It is assumed that the surface oxide layer fractured at a stress lower than the yield stress, which caused sharp cracks to form, and consequently accelerated yield by forming stress concentrations. The ultimate stress, however, was lower for the KTL sample (σ_u=373.9 MPa compared to 383.4 MPa for the Ti uncoated sample). This was also evident from the curve for KTL in Figure 4.1, which dropped more rapidly than those for the other samples. This indicates that work hardening during plastic deformation was less effective than for the other samples, which could to be connected to the changes observed in grain structure.

5.2 Surface Roughness

Before assessing the observed surface roughness in terms of fatigue results, it must be considered whether surface roughness is as relevant for coated samples as for the uncoated ones. For the KTL samples, critical cracks initiate not in the coating, but rather in the underlying aluminium surface. For the surface roughness measured for the KTL samples to be relevant, it follows that the roughness would have to be correlated between the aluminium and the coating. This is probably not the case. Notice that the average values shown in Table 4.3 supports this, as the mean R_{max} value for KTL was considerably lower than the one for uncoated samples. For the anodised samples it is not clear whether the anodised layer cracked immediately upon exposure to the cyclic stress environment, or if some number of cycles were required. If the first is true, the surface roughness would be irrelevant. If one assumes the latter, however, the surface roughness also for these samples would be expected to impact the fatigue properties to some degree. From the admittedly few points shown in Figure 4.8, this could be interpreted as to be the case, as 2 out of 3 anodised series in air show the expected correlation. However, this is not enough data to draw a definite conclusion.

The maximum surface roughness to number of cycles to failure found for samples fatigue tested in air and in 5 wt% NaCl are shown in Figures 4.8 and 4.9, respectively. Higher surface roughness is expected to correlate with fewer cycles to failure. For the samples tested in 5 wt% NaCl, true correlations are only found for 2 of the 12 series. Corrosion probably played a dominant part in crack initiation, and overshadowed the effects of surface roughness. For the samples fatigue tested in air, the correlation is true for 5 out of 8 series, and partially for 2 of the remaining 3. Although the observed correlation for the KTL samples is probably coincidental, the general correlation appears to show that surface roughness was an important contributor to fatigue failures in air.

At this point, it should be noted that surface roughness was measured for each of the 4 surfaces in the parallel area for each sample, but the corners were not measured. Also, most fractures were found to have initiated in the corners. It follows that if a surface flaw directly contributed to crack initiation, it was most likely in or close to a corner, and therefore not measured. This considered, the observed correlation between measured maximum surface flaw size and fatigue life is surprising.

It appears that some sort of correlation exists between the surface roughness measured in the surfaces and the roughness of the corners. Therefore, it is perceivable that the average roughness (R_a) might be more influential than the maximum roughness (R_{max}). When a measured imperfection leads to crack initiation, R_{max} is expected to influence the number of cycles to failure. If an unmeasured corner flaw gives crack initiation, however, the R_a might be a better measure, as a sample with higher average roughness may be more likely to have a more prominent flaw in a corner. However, as seen from Figures 4.10 and 4.11, no such correlation was found between R_a and N_f. Therefore, it is probable that R_{max} was more influential.

The average values for R_a and R_{max} (shown in Table 4.3) both demonstrate that KTL samples were less rough than uncoated samples, who again were less rough than anodised samples. It may be worth noting that this relationship correlates with the observed fatigue life. KTL samples endured more cycles than uncoated samples, who again endured more than anodised ones. However, as explained earlier, the difference in surface roughness is probably not the main reason for the observed differences in fatigue life between differently coated samples.

The measured surface roughness of the KTL samples did probably not influence their fatigue performance. However, this may change when the coating is scratched. The investigation of one such scratch shown in Figure 2.2 and the W_{max} value in Table 4.4 indicates a 32 µm deep scratch. When seen in combination with the coating thickness of 21.8 µm shown in Figure 4.4 for KTL samples, this indicates that the scratch penetrated the aluminium surface and produced a scratch of approximately 10 µm. Note, however, that this scratch is rather gradually penetrating the aluminium. Thus, the flaw created is not very sharp, and not expected to create particularly influential stress concentrations.

5.3 S-N Curves

The S-N curve for samples fatigue tested in air shown in Figure 4.13 clearly shows that anodised samples failed after the fewest cycles, and that KTL samples endured more cycles than uncoated ones. These differences are clear both at 160 and 220 MPa. The anodised samples failed in average after only about 25 % (at 160 MPa) and 40 % (at 220 MPa) as many cycles as the uncoated ones. Meanwhile, the KTL samples endured on average about

37 % and 39 % more cycles than the uncoated ones at 160 and 220 MPa, respectively. Notice, however, how the line for the uncoated samples approaches the one for KTL at 160 MPa. This should be seen in combination with the fact that many more uncoated samples were tested, and that they were also tested at lower stresses, yielding more run-outs. The representation of the expected number of cycles per cyclic stress amplitude as a straight line is an approximation, the relationship should really be a curved line, like the one in Figure 2.5. Therefore, the observed increase in fatigue life for uncoated samples compared to KTL samples at low stresses is exaggerated.

This considered, coating with KTL significantly improved the fatigue strength in air, for all stress amplitudes. It is suggested that the ductile surface coating shielded the underlying aluminium from the highest stress amplitudes in the surface, thereby inhibiting critical crack initiation, and improving fatigue life. Notice also the points for Ti anodised and Ti uncoated, which were both tested only at 160 MPa in air. The Ti anodised samples showed a slight increase in fatigue life compared to anodised samples with no extra Ti. However, as only 2 and 3 of these samples were tested at 220 MPa, the uncertainty of this is considerable. The fatigue life for Ti uncoated samples was approximately equal to that of uncoated samples, implying no effect of the Ti additions.

The results for samples tested in air may be compared to those from the previous work, shown in Figure 3.5. It appears that the uncoated samples there endured fewer cycles at 220 MPa, while the number of cycles at 160 MPa were more or less the same. Still, the numbers of cycles at 220 MPa differed only from about 30-40 000 to 50-60 000. Considering only two samples were tested at each time, this difference is not significant. Also, from the reference curves from SINTEF, in Figure 3.3, we see that both lie within the expected range for this material at 220 MPa. The same is true for the measurements at 160 MPa.

The S-N curves for samples fatigue tested in 5 wt% NaCl shown in Figure 4.14 show similar relationships. The anodised samples, with and without extra titanium, demonstrate approximately equal fatigue life, both considerably lower than uncoated samples. The Ti uncoated samples performed slightly better than those without extra Ti, especially at 220 MPa. However, it is important to keep in mind the statistical nature of fatigue (see Chapter 2.7.11). Considering that only 7 uncoated and 5 Ti uncoated samples were tested in corrosion fatigue in total, the relatively small superiority observed for Ti uncoated must be viewed as uncertain. The KTL samples significantly outperformed all other sample types, as long as the coating was undamaged. At 160 MPa, these samples endured in average about 413 % more cycles than uncoated ones. For the scratched KTL samples, the observed fatigue life was not as good as those of unscratched KTL samples. Still, they outperformed the uncoated samples with 43 % in average at 160 MPa. Note, from Figure 4.12, that the total damage area of the coating in the scratched samples is considerable. This explains the drop in fatigue life compared to unscratched samples, and enhances the impression that even a damaged KTL coating significantly protects the material.

The corrosion fatigue lines in Figure 4.14 may be compared to the corrosion fatigue data supplied by SINTEF, which are shown in Figure 3.4. Notice that these tests were done at R=0.1, so conversions were necessary before comparisons could be made. Through Equations 2.10-2.12, it is clear that σ_a=72 MPa at R=0.1 corresponds to σ_{max}=160 MPa. Similarly, σ_a=99 MPa at R=0.1 corresponds to σ_{max}=220 MPa. Recall that at R=-1, σ_{max}=σ_a, so the maximum stresses in the reference are the same as those used in this thesis. Recall, however, that the expected number of cycles to failure is lower for higher R-values, when σ_{max} is the same (see Chapter 2.7.8). Therefore, corrections were made using the SWT equation and the Basquin law. The corrected S-N curve in Figure 4.15 is a conservative estimate, due to the use of the SWT equation, so the numbers of cycles shown are on the low end of what should be expected. Recall also that the Basquin law is valid in the high cycle regime. The fatigue lives indicated, especially at 220 MPa, appear to be in the transition regime between low and high cycle fatigue.

The series in Figure 4.15 labelled cutting edge and machined w/smoothened edges may be seen as extremes in the way of high and low surface roughness, respectively. The uncoated samples in this thesis are expected to perform intermediary compared to these reference series. At 220 MPa, the reference data range from N_f=10 000 to N_f=20 000 cycles to failure, approximately. The uncoated samples tested here in corrosion fatigue range roughly from 20 to 30 000. Thus, considering the conservative estimate that was made for the number of cycles, these values appear to match the expectations. At 160 MPa, the reference ranges from about 30 000 to 100 000, while the results here were about 60 000 to 130 000. Again, the results appear to be in the expected range, once the conservative estimate is considered.

The applied stress amplitudes of 160 and 220 MPa are relatively low, considering the yield stress, which was found to be about 320-330 MPa. These were chosen to test the samples in the high cycle fatigue regime. The range of number of cycles to failure was roughly from 2×10^4 to 10^6, when fatigue tests both in air and in 5 wt% NaCl were considered. Thus, the lowest fatigue lives probably lie in the transitional area between the low and high cycle fatigue regimes. It is known that the low cycle regime is governed by plastic deformations, and that crack propagation plays a larger role than in the high cycle regime. The mechanisms controlling fatigue in the two regimes are significantly different, which is why it is important to understand which fatigue regime is most influential for each application. It is not given that the conclusions from this work also apply in the low cycle regime, and investigations in the low cycle fatigue regime are recommended.

5.4 Fracture Surfaces

The investigated fracture surfaces of samples fatigue tested in air are similar for the KTL sample and the Ti uncoated sample, as can be seen from Figures 4.16 and 4.17. For both samples, a critical crack was found to have initiated in a corner, close to a smooth area. Such smooth areas were found in most samples. It is proposed that this smooth area could be some particle or chip, incorporated during machining of the samples. This implies that machining was responsible for most critical crack initiations in uncoated samples. Investigations of the nature of these smooth areas are recommended. In the Ti anodised sample, multiple crack initiation points were observed along the lower edge, as shown in Figure 4.18. It is assumed that the brittle surface oxide layer cracks after few cycles. This enhances the stress concentration along the edges and accelerates crack initiation. This is supported both by the occurrence of several crack initiations and by the propagation direction in Figure 4.18 (c). If the surface is cracked along the edge, this crack may grow evenly into the aluminium, yielding the indicated crack propagation direction.

For the fracture surfaces of samples fatigue tested in 5 wt% NaCl, some signs of corrosion were identified. Signs of intergranular fracture were found in the uncoated sample, as shown in Figure 4.19 (d). This is seen from the pattern reminiscent of the grain structure of the material. This was unlike any examined fracture surfaces from samples fatigue tested in air, which supports the belief that it was most likely a result of corrosive reactions. Some amount of IGC probably occurred, weakening the grain boundaries. This implies that the saltwater solution had a negative effect on the crack propagation rate.

Grain-like patterns were also identified in some of the edges, like the initiation point shown in Figure 4.20. Note that this was the uncoated sample that endured the highest number of cycles, and where corrosion had most time to affect the material. This grain-like area is another feature not found in the samples tested in air, and is therefore most likely caused by corrosion. These corrosive attacks are also most likely IGC, at least in part, as weakened grain boundaries would explain the aforementioned appearance.

For the scratched KTL sample shown in Figure 4.22, two crack initiation sites were identified. One in a corner, where a smooth area was identified, and one smaller along the bottom edge. The latter initiation site lies close to one of the inscribed scratches. This shows that the scratch decreased the fatigue life of this sample, as supported by the corrosion fatigue results. Recall that the scratch penetrated about 10 µm into the aluminium, thus the surface roughness increase is noteworthy. However, the crack did not initiate directly from the scratch, but rather in its vicinity. Corrosive solution most likely penetrated the coating at the scratch. This caused nearby corrosive reactions to damage the surface, which created stress concentrations that led to crack initiation.

5.5 Real Life Applicability

Before applying the results of test sample investigations to the full-size component produced by Benteler, several differences need to be considered. Most obviously, the component is considerably larger and more complex geometrically than the samples tested here. The making of such a complex component requires extensive machining, significantly exceeding what is required for test samples. It was proposed that machining was responsible for most crack initiations in uncoated samples, by incorporating brittle chips into the corners of the samples. The likelihood of such chip incorporation would be expected to increase for the full-size component, as more machining is performed. However, that is only true if the machining in the industrial process at Benteler is similar to the machining of the test samples as performed by SINTEF, which is not necessarily the case. This could be investigated by analysing fracture surfaces of fatigue tested full-size components.

Recall that an effect of adding Ti to the alloy was proposed to be increased machinability by induced chip breaking, making the chips easier to extract away from the cutting front (see Chapter 2.2.1). Therefore, although the observed effect of alloying with Ti in this thesis was small at best, similar additions could potentially cause a more pronounced effect in the full-size component. Experiments with the full-size component are, again, recommended.

For samples with KTL coating, an increase in the fatigue and corrosion fatigue strength of the test samples was observed, even after the introduction of scratches. This makes coating with KTL a promising option for the component. However, some recrystallisation was observed at the interface between aluminium and coating. This thin layer was not assumed to have affected the fatigue properties of the test samples, and it is not expected to affect the component any more severely, as the thickness is the same. However, investigations should be made of the grain structure of the component after coating, to make sure no undesirable microstructural changes occur.

The stress mode for the component is bending, while the test samples were stressed in tension. Recall that materials exposed to bending are expected to have increased fatigue life compared to those exposed to tensile stresses (see Chapter 2.7.9). However, the size of the component means this effect is weakened, as the stress decreases more gradually throughout the material (see Chapter 2.7.10). These effects are best investigated through fatigue testing of the full-size component in bending.

The frequency is another important difference between test samples and full-size component (see Chapter 2.7.7). The component is expected to experience a much lower stress frequency compared to the test samples. Although this is not expected to influence aluminium in air, corrosive reactions occurring from saltwater from roads will have more time to affect the component compared to the submerged test samples. This is expected to decrease fatigue life for the component compared to samples tested in corrosion fatigue. This effect could be minimised by coating with KTL. Even if the coating is breached, the available area for corrosion to occur will be small, decreasing the expected corrosive reactions. It should be noted, however, that the component in real life is not expected to be exposed to saltwater for the entirety of its service life, which is expected to somewhat decrease the effects of corrosion.

Similarly, the stress amplitude and mean stress in real life is expected to be different from the laboratory conditions. The mean stress is expected to be higher than zero, which would give more cycles to failure (see Chapter 2.7.8). The stress amplitude is less predictable, as it depends on the surface conditions of the road, speed of the car, etc. Also, it is not obvious whether many small applications of stress or fewer larger applications are most influential in real life failures of the component. If the latter is true, the low cycle fatigue regime would be more important to understand. Which regime is most influential could be investigated by analysing the fracture surface of a component fractured in service. The number of cycles to failure can be approximated through measurements of striation spacing (see Chapter 2.10.3).

6. Conclusions

The corrosion fatigue properties of a 6082 aluminium alloy heat treated to T6x were investigated. Uncoated, anodised and organically coated (KTL) samples were tested. Additionally, some uncoated and anodised samples with extra Ti added were tested. All sample types were tested at R=-1 both in air and in 5 wt% NaCl. Some KTL samples were scratched before testing in 5 wt% NaCl. Mechanical properties, microstructures, coating thickness, surface roughness and fracture surfaces were also investigated.

For uncoated samples, the 5 wt% NaCl solution was found to increase both crack initiation and crack propagation rates. This was supported by corrosive attacks found as crack initiation points, and signs of intergranular fracture that was apparently caused by IGC.

Alloying with extra Ti was not found to increase fatigue or corrosion fatigue resistance significantly, nor affect grain structure. A slight increase in yield strength and ultimate stress was observed. Increased machinability had been reported for 6xxx alloys with extra Ti, but no evidence of this was found. It was suggested that this effect may be more evident in the full-size component. Further work is required before a conclusion can be made as to whether alloying with extra Ti improves the fatigue and/or corrosion fatigue resistance of the component.

Anodising was found to accelerate fatigue, both in air and in 5 wt% NaCl. The average fatigue life at 160 MPa was only 25 % in air and 40 % in 5 wt% NaCl, relative to uncoated samples. A similar decrease was seen also with extra Ti in the alloy. It was suggested that the surface oxide layer of the anodised samples cracked early during cyclic loading, causing stress concentrations that accelerated crack initiation in the aluminium.

The KTL coating was found to protect against fatigue, both in air and in 5 wt% NaCl. An increase in average fatigue life of 37 % in air and 413 % in 5 wt% NaCl was observed for KTL at 160 MPa. A thin recrystallised layer was found in the edge, but this did probably not decrease fatigue resistance. Fracture surface investigations revealed corrosive attacks in the scratched samples, but their fatigue life was still superior to uncoated samples. An average of 43 % more cycles than uncoated samples were endured at 160 MPa. The coating was suggested to shield the aluminium surface from the highest stress concentrations, thereby impeding crack initiation, in addition to preventing corrosive reactions. Based on these results, coating of the component with KTL was recommended.

6.1 Suggested Further Work

Some elements worthy of further investigations were identified. These are listed below.

- Chemical analysis of the smooth areas found close to most crack initiation sites in corners.
- Investigations of the mechanisms concerning crack initiation.
- Investigations of the effects of KTL in the low cycle fatigue regime.
- Fatigue testing of the full-size component in bending fatigue.
- Testing of the full-size component with Ti additions.
- Investigations of full-size component grain structure after KTL coating.
- Investigations of service failures of full-size components, to approximate the number of cycles to failure and determine the most influential fatigue regime.

References

[1] G. E. Dieter. ‘Fatigue of Metals’. In: Mechanical Metallurgy. Mc Graw-Hill Book Company, 1988, pp. 375–431.

[2] I. Milne, R. Ritchie and B. Karihaloo. ‘Cyclic Loading and Fatigue’. In: Comprehensive Structural Integrity. Vol. 4. Elsevier, 2003. Chap. Corrosion Fatigue, pp. 345–358.

[3] A. Almar-Naess, T. Moan, P. J. Haagensen et al. ‘Investigation of the Alexander L. Kielland Failure- Metallurgical and Fracture Analysis’. In: *Journal of Energy Resources Technology* 106 (1984), pp. 24–31.

[4] J. K. Solberg. ‘Aluminium og Aluminiumslegeringer’. In: Teknologiske Metaller og Legeringer. Institutt for Materialteknologi, 2014, pp. 191–242.

[5] I. J. Polmear. ‘Wrought Aluminium Alloys’. In: Light Alloys: From Traditional Alloys to Nanocrystals. Elsevier, 2005, pp. 97–204.

[6] K. Newton, W. Steeds and T. K. Garrett. ‘Suspension Principles’. In: The Motor Vehicle. Butterworth-Heinemann, 1996, pp. 931–963.

[7] N. Birbilis and B. Hinton. ‘Corrosion and Corrosion Protection of Aluminium’. In: Fundamentals of Aluminium Metallurgy: Production, Processing and Applications. Ed. by R. Lumley. Elsevier Science & Technology, 2010, pp. 574–604.

[8] A. M. Cree, G. W. Weidmann and R. Hermann. ‘Film-Assisted Fatigue Crack Propagation in Anodized Aluminium Alloys’. In: *Journal of Materials Science Letters* 14 (1995), pp. 1505–1507.

[9] W. D. Callister Jr. and D. R. Rethwisch. ‘Mechanical Properties of Metals’. In: Materials Science and Engineering. Wiley, 2015, pp. 208–252.

[10] W. D. Callister Jr. and D. R. Rethwisch. ‘Properties and Applications of Metals’. In: Materials Science and Engineering. Wiley, 2015, pp. 432–459.

[11] M. Easton, D. H. StJohn and L. Sweet. 'Grain Refinement and Hot Tearing of Aluminium Alloys - How to Optimise and Minimise'. In: Aluminium Cast House Technology XI. Vol. 630. Materials Science Forum. Trans Tech Publications, Jan. 2010, pp. 213–221.

[12] J. Zander and R. Sandström. 'Modelling Technological Properties of Commercial Wrought Aluminium Alloys'. In: *Materials & Design* 30.9 (2009), pp. 3752–3759.

[13] J. L. Jorstad. 'Selection of Alloys'. In: Aluminium Permanent Mold Handbook. American Foundry Society, 2001, pp. 3–10.

[14] A. R. Froehlich, R. C. Jacques, T. R. Strohaecker et al. 'The Correlation of Machinability and Microstrutural Characteristics of Different Extruded Aluminum Alloys'. In: *Journal of Materials Engineering and Performance* 16.6 (Dec. 2007), pp. 784–791.

[15] MakeItFrom.com. *6082-T6 Aluminum.* URL: `https://www.makeitfrom.com/material-properties/6082-T6-Aluminum` (visited on 04/06/2019).

[16] matweb.com. *Aluminium 6082-T6.* URL: `http://www.matweb.com/search/datasheet_print.aspx?matguid=fad29be6e64d4e95a241690f1f6e1eb7` (visited on 04/06/2019).

[17] A. Materials. *Aluminium Alloy 6082.* URL: `https://www.aircraftmaterials.com/data/aluminium/6082.html` (visited on 04/06/2019).

[18] N. Aluminium. *Alloy Data Sheet EN AW-6082 [AlSi1MgMn].* URL: `https://www.nedal.com/wp-content/uploads/2016/11/Nedal-alloy-Datasheet-EN-AW-6082.pdf` (visited on 04/06/2019).

[19] W. D. Callister Jr. and D. R. Rethwisch. 'Fabrication and Processing of Engineering Materials'. In: Materials Science and Engineering. Wiley, 2015, pp. 584–637.

[20] R. Cayless. 'Alloy and Temper Designation Systems for Aluminum and Aluminum alloys'. In: ASM Handbook. ASM International, 1990, pp. 15–28.

[21] W. D. Callister Jr. and D. R. Rethwisch. 'Corrosion and Degradation of Materials'. In: Materials Science and Engineering. Wiley, 2015, pp. 638–679.

[22] K. S. Rao and K. P. Rao. 'Pitting Corrosion of Heat-Treatable Aluminium Alloys and Welds: A Review'. In: *Transactions of the Indian Institute of Metals* 57.6 (2004), pp. 593–610.

[23] J. Lyndon, R. Gupta, M. Gibson et al. 'Electrochemical Behaviour of the β-Phase Intermetallic (Mg2Al3) as a Function of pH as Relevant to Corrosion of Aluminium-Magnesium Alloys'. In: *Corrosion Science* 70 (May 2013), pp. 290–293.

[24] G. Svenningsen, J. E. Lein, A. Bjørgum et al. 'Effect of Low Copper Content and Heat Treatment on Intergranular Corrosion of Model AlMgSi Alloys'. In: *Corrosion Science* 48 (Jan. 2006), pp. 226–242.

[25] J. M. Runge. 'Anodic Aluminum Oxide Growth and Structure'. In: The Metallurgy of Anodizing Aluminum. Springer, Cham, 2018, pp. 281–320.

[26] J. M. Runge. 'Anodizing as an Industrial Process'. In: The Metallurgy of Anodizing Aluminum. Springer, Cham, 2018, pp. 149–190.

[27] H. Ohshima. 'Electrophoresis'. In: Reference Module in Chemistry, Molecular Sciences and Chemical Engineering. Elsevier, 2016.

[28] L. Besra and M. Liu. 'A Review on Fundamentals and Applications of Electrophoretic Deposition (EPD)'. In: *Progress in Materials Science* 52.1 (2007), pp. 1–61. URL: `http://www.sciencedirect.com/science/article/pii/S0079642506000387`.

[29] B. N. Popov. 'Organic Coatings'. In: Corrosion Engineering. Ed. by B. N. Popov. Amsterdam: Elsevier, 2015, pp. 557–579.

[30] E. Oberg, F. D. Jones, H. L. Horton et al. 'Definitions of Terms Relating to the Measurement of Surface Texture'. In: Machinery's Handbook (29th Edition). Industrial Press, 2012.

[31] E. Csanády and E. Magoss. 'Surface Roughness'. In: Mechanics of Wood Machining. Springer, Berlin, Heidelberg, 2013, pp. 167–194.

[32] G. W. Stachowiak and A. W. Batchelor. 'Fundamentals of Contact Between Solids'. In: Engineering Tribology. Elsevier Science, 1993, pp. 527–556.

[33] W. D. Callister Jr. and D. R. Rethwisch. 'Failure'. In: Materials Science and Engineering. Wiley, 2015, pp. 285–328.

[34] F. Briffod, T. Shiraiwa and M. Enoki. 'Fatigue Crack Initiation Simulation in Pure Iron Polycrystalline Aggregate'. In: *Materials Transactions* 57.10 (2016), pp. 1741–1746.

[35] S. Majumdar and J. D. Morrow. 'Correlation Between Fatigue Crack Propagation and Low Cycle Fatigue Properties'. In: *National Technical Information Service U. S. Department of Commerce* (Apr. 1973).

[36] S. Suresh. 'Stress-Life Approach'. In: Fatigue of Materials. Cambridge University Press, 1998, pp. 221–255.

[37] N. E. Dowling. 'Stress-Based Approach to Fatigue: Notched Members'. In: Mechanical Behaviour of Materials. Pearson, 2013, pp. 491–559.

[38] S. Suresh. 'Small Fatigue Cracks'. In: Fatigue of Materials. Cambridge University Press, 1998, pp. 541–569.

[39] C. Villalobos-Gutiérrez, G. Gedler-Chacón, J. L. Barbera-Sosa et al. 'Fatigue and Corrosion Fatigue Behavior of an AA6063-T6 Aluminum Alloy Coated with a WC–10Co–4Cr Alloy deposited by HVOF thermal spraying'. In: *Surface and Coatings Technology* 202.18 (2008), pp. 4572–4577.

[40] C. M. Sonsino, A. Berg-Pollack and V. Grubisic. 'Structural Durability Proof of Automotive Aluminium Safety Components - Present State of the Art'. In: SAE 2005 World Congress & Exhibition. SAE International, Apr. 2005.

[41] J. Xie, A. T. Alpas and D. O. Northwood. 'A Mechanism for the Crack Initiation of Corrosion Fatigue of Type 316L Stainless Steel in Hank's Solution'. In: *Materials Characterization* 48.4 (2002), pp. 271–277.

[42] N. E. Dowling. 'Fatigue of Materials: Introduction and Stress-Based Approach'. In: Mechanical Behaviour of Materials. Pearson, 2013, pp. 416–490.

[43] R. G. Budynas and J. K. Nisbett. 'Fatigue Failure Resulting from Variable Loading'. In: Shingley's Mechanical Engineering Design. McGraw-Hill, 2011, pp. 265–357.

[44] W. D. Callister Jr. and D. R. Rethwisch. 'Imperfections in Solids'. In: Materials Science and Engineering. Wiley, 2015, pp. 143–179.

[45] J. Schinderlin, I. Arganda-Carreras, E. Frise et al. 'Fiji: An Open-Source Platform for Biological-Image Analysis'. In: *Nature Methods* 9 (2012), pp. 676–682.

[46] J. Hjelen. 'Elektronoptikk'. In: Scanning Elektron-Mikroskopi. Metallurgisk institutt, NTH, 1989, pp. 2–22.

[47] V. Randle. 'Electron Backscatter Diffraction: Strategies for Reliable Data Acquisition and Processing'. In: *Materials Characterization* 60.9 (Sept. 2009), pp. 913–922.

[48] J. Hjelen. 'Fraktografi - Metalliske Materialer'. In: Scanning Elektron-Mikroskopi. Metallurgisk institutt, NTH, Aug. 1989, pp. 86–93.

[49] G. E. Dieter. 'Fracture'. In: Mechanical Metallurgy. Mc Graw-Hill Book Company, 1988, pp. 241–272.

[50] Corrosionpedia. *Beach Marks.* URL: `https://www.corrosionpedia.com/definition/146/beach-marks` (visited on 04/06/2019).

[51] S. Suresh. 'Fatigue Crack Growth in Ductile Solids'. In: Fatigue of Materials. 10. Cambridge University Press, 1998, pp. 331–382.

[52] D. McIntyre. 'Fractographic Analysis of Fatigue Failures'. In: *Journal of Engineering Materials and Technology* 75 (1975), pp. 194–205.

[53] G. T. Lindstad. 'Corrosion Fatigue of Extruded AA6082 Aluminium Alloy - The effects of Surface Roughness: Machined, Punched, and Counter Trimmed Surfaces'. MA thesis. NTNU, 2017.

A. Appendix

A.1 Fatigue Results

Table A.1: Fatigue results from samples tested in air.

	σ_a [MPa]	N$_f$		σ_a [MPa]	N$_f$
Uncoated	140	257268	Anodised	160	45772
	140	1145097		160	50473
	140	1250803		160	60520
	150	313802		220	22433
	160	164794		220	22626
	160	164846			
	160	182824	KTL	160	143990
	160	191552		160	224089
	160	321386		160	472188
	170	134219		220	75702
	170	137979		220	78722
	180	104203			
	180	117955	Ti Uncoated	160	220428
	180	156018		160	251575
	190	89750		160	253281
	200	60993			
	210	53044	Ti Anodised	160	54372
	220	50149		160	61561
	220	61020		160	63284

Table A.2: Fatigue results from samples tested in 5 wt% NaCl.

	σ_a [MPa]	N$_f$		σ_a [MPa]	N$_f$
Uncoated	160	61922	Anodised	160	28353
	160	90631		160	29007
	160	100192		160	35638
	160	129918		160	60466
	220	16714		220	14721
	220	25250		220	15418
	220	29424		220	18672
KTL	160	139926	KTL Scratched	160	84125
	160	210211		160	98845
	160	1121208		160	133396
	220	35745		160	231831
	220	55460		220	33091
				220	40615
Ti Uncoated	160	98064	Ti Anodised	160	31054
	160	98985		160	40191
	160	119744		160	49547
	220	26324		220	15748
	220	41316		220	18508

A.2 Surface Roughness

Table A.3: Results of surface roughness measurements.

Sample type	Nr.	Side	Ra [µm]	Rq [µm]	Rt [µm]	Rz [µm]	Rmax [µm]
KTL	61	down	0,60	0,75	5,45	4,20	5,32
KTL	61	side 1	0,57	0,72	5,60	4,14	5,60
KTL	61	side 2	0,56	0,72	6,13	4,44	5,83
KTL	61	up	0,64	0,81	5,91	4,61	5,38
KTL	62	down	0,71	0,89	6,30	5,01	6,26
KTL	62	side 1	0,54	0,69	4,81	3,88	4,81
KTL	62	side 2	0,55	0,71	5,51	4,42	5,25
KTL	62	up	0,69	0,87	6,09	4,87	6,09
KTL	63	down	0,62	0,79	6,63	4,92	6,21
KTL	63	side 1	0,56	0,72	4,89	4,10	4,35
KTL	63	side 2	0,53	0,66	4,50	3,88	4,50
KTL	63	up	0,60	0,78	7,80	4,81	6,67
KTL	64	down	0,62	0,83	7,03	5,57	6,50
KTL	64	side 1	0,57	0,72	4,64	4,11	4,64
KTL	64	side 2	0,57	0,72	4,27	3,78	4,04
KTL	64	up	0,63	0,78	5,74	4,40	5,58
KTL	67	down	0,62	0,79	5,65	4,75	5,34
KTL	67	side 1	0,63	0,79	6,09	4,44	5,43
KTL	67	side 2	0,71	1,01	10,38	6,50	10,38
KTL	67	up	0,71	0,91	6,78	5,42	6,13
KTL	68	down	0,63	0,80	6,80	4,96	5,38
KTL	68	side 1	0,61	0,77	4,99	4,32	4,65
KTL	68	side 2	0,63	0,80	5,07	4,36	5,07
KTL	68	up	0,59	0,75	5,63	4,33	5,13
KTL	69	down	0,67	0,83	5,59	4,35	5,08
KTL	69	side 1	0,58	0,73	5,38	4,07	4,83
KTL	69	side 2	0,65	0,85	5,87	4,70	5,87
KTL	69	up	0,62	0,78	5,90	4,85	5,90
KTL	71	down	0,68	0,87	6,92	4,82	5,80
KTL	71	side 1	0,57	0,72	4,96	3,89	4,21
KTL	71	side 2	0,43	0,53	3,65	2,82	3,31
KTL	71	up	0,64	0,79	5,29	4,42	5,05
KTL	72	down	0,70	0,89	8,07	5,49	7,33
KTL	72	side 1	0,56	0,72	6,06	4,26	5,01
KTL	72	side 2	0,46	0,59	4,19	3,34	4,19
KTL	72	up	0,61	0,77	6,35	4,90	5,80
KTL	73	down	0,58	0,74	4,98	4,23	4,98
KTL	73	side 1	0,50	0,64	5,16	3,79	4,98
KTL	73	side 2	0,56	0,70	4,84	3,78	4,62
KTL	73	up	0,66	0,85	6,52	5,02	6,47
KTL	74	down	0,67	0,84	6,17	4,95	5,39
KTL	74	side 1	0,57	0,73	4,80	4,07	4,80
KTL	74	side 2	0,60	0,78	5,81	4,87	5,31
KTL	74	up	0,60	0,76	6,60	4,52	6,20

Sample type	Nr.	Side	Ra [µm]	Rq [µm]	Rt [µm]	Rz [µm]	Rmax [µm]
KTL	75	down	0,70	0,88	5,76	4,88	5,40
KTL	75	side 1	0,49	0,61	3,83	3,30	3,63
KTL	75	side 2	0,62	0,78	5,58	4,42	5,06
KTL	75	up	0,66	0,83	5,72	4,71	5,55
KTL	76	down	0,68	0,88	6,62	5,35	6,62
KTL	76	side 1	0,55	0,69	4,70	3,97	4,69
KTL	76	side 2	0,58	0,73	4,78	4,13	4,74
KTL	76	up	0,68	0,85	5,30	4,65	5,30
KTL	77	down	0,71	0,89	7,56	5,02	6,74
KTL	77	side 1	0,55	0,69	4,34	3,60	4,07
KTL	77	side 2	0,51	0,65	4,52	3,78	4,31
KTL	77	up	0,67	0,89	9,79	5,37	9,23
KTL	78	down	0,48	0,61	4,60	3,34	4,60
KTL	78	side 1	0,49	0,62	4,37	3,40	4,18
KTL	78	side 2	0,46	0,59	4,02	3,41	3,93
KTL	78	up	0,60	0,77	7,05	4,81	6,29
KTL	80	down	0,55	0,71	4,77	3,85	4,34
KTL	80	side 1	0,61	0,76	5,43	4,24	5,03
KTL	80	side 2	0,59	0,75	5,02	4,25	4,92
KTL	80	up	0,71	0,89	5,83	4,96	5,43
Uncoated	101	down	1,00	1,28	9,20	6,94	9,13
Uncoated	101	side 1	0,68	0,86	6,12	4,52	6,12
Uncoated	101	side 2	0,67	0,87	5,99	5,00	5,70
Uncoated	101	up	0,87	1,11	6,86	6,15	6,49
Uncoated	102	down	0,86	1,13	8,37	6,14	7,88
Uncoated	102	side 1	0,63	0,79	5,67	4,33	5,66
Uncoated	102	side 2	0,68	0,86	5,28	4,61	5,28
Uncoated	102	up	0,79	1,00	7,33	5,48	6,82
Uncoated	103	down	0,77	0,98	6,06	5,04	6,05
Uncoated	103	side 1	0,69	0,89	6,72	5,07	6,64
Uncoated	103	side 2	1,10	1,42	10,13	7,75	9,50
Uncoated	103	up	0,88	1,11	7,52	5,84	7,52
Uncoated	104	down	0,74	0,93	6,71	5,45	5,97
Uncoated	104	side 1	0,64	0,82	5,45	4,56	5,05
Uncoated	104	side 2	0,57	0,72	5,19	4,03	4,61
Uncoated	104	up	1,01	1,30	9,01	6,96	9,01
Uncoated	105	down	0,80	1,01	7,08	5,52	6,72
Uncoated	105	side 1	0,85	1,07	7,03	5,85	7,03
Uncoated	105	side 2	0,59	0,75	4,86	4,19	4,86
Uncoated	105	up	0,99	1,28	10,70	7,70	8,97
Uncoated	106	down	0,80	1,02	7,17	5,86	6,85
Uncoated	106	side 1	0,65	0,85	6,10	4,90	6,10
Uncoated	106	side 2	0,64	0,80	5,50	4,30	5,25
Uncoated	106	up	1,00	1,33	10,18	7,10	10,18
Uncoated	107	down	0,94	1,16	6,72	6,12	6,63
Uncoated	107	side 1	0,64	0,80	6,34	4,16	5,69
Uncoated	107	side 2	0,60	0,76	5,25	4,09	5,23
Uncoated	107	up	0,78	1,00	7,03	5,76	7,03

Sample type	Nr.	Side	Ra [µm]	Rq [µm]	Rt [µm]	Rz [µm]	Rmax [µm]
Uncoated	108	down	0,78	0,99	5,92	4,99	5,72
Uncoated	108	side 1	0,56	0,70	4,17	3,53	4,17
Uncoated	108	side 2	0,57	0,71	4,18	3,57	4,10
Uncoated	108	up	1,17	1,52	11,46	8,99	11,46
Uncoated	109	down	0,76	0,97	7,19	5,44	6,54
Uncoated	109	side 1	0,69	0,90	5,98	4,90	5,91
Uncoated	109	side 2	0,67	0,87	7,39	4,81	6,56
Uncoated	109	up	0,85	1,08	6,69	6,00	6,49
Uncoated	110	down	1,01	1,25	8,24	6,58	7,27
Uncoated	110	side 1	0,66	0,86	7,37	5,16	5,86
Uncoated	110	side 2	0,62	0,79	5,40	4,23	5,40
Uncoated	110	up	1,06	1,35	8,42	7,43	8,34
Uncoated	131	down	0,92	1,25	10,64	6,84	10,64
Uncoated	131	side 1	0,57	0,71	4,68	3,93	4,21
Uncoated	131	side 2	0,58	0,76	5,86	4,59	5,45
Uncoated	131	up	0,91	1,20	11,05	6,80	11,05
Uncoated	132	down	0,86	1,14	9,34	6,97	8,13
Uncoated	132	side 1	0,59	0,71	3,93	3,45	3,82
Uncoated	132	side 2	0,57	0,72	5,59	4,07	4,61
Uncoated	132	up	0,72	0,92	6,12	4,77	6,12
Uncoated	133	down	0,74	0,94	6,53	5,66	6,48
Uncoated	133	side 1	0,58	0,74	4,71	3,96	4,59
Uncoated	133	side 2	0,61	0,76	4,48	3,82	4,37
Uncoated	133	up	0,80	1,01	6,66	5,53	6,63
Anodised	141	down	1,18	1,50	9,42	8,15	9,09
Anodised	141	side 1	1,67	2,08	12,27	10,84	11,65
Anodised	141	side 2	1,54	1,94	11,38	9,81	11,38
Anodised	141	up	1,33	1,64	10,37	8,81	10,37
Anodised	142	down	1,28	1,62	10,49	9,08	10,26
Anodised	142	side 1	1,62	2,12	18,26	11,95	18,26
Anodised	142	side 2	1,42	1,78	10,87	9,45	10,42
Anodised	142	up	1,15	1,42	9,66	7,73	8,67
Anodised	143	down	1,27	1,60	10,89	9,32	10,49
Anodised	143	side 1	1,57	2,02	17,14	11,75	17,06
Anodised	143	side 2	1,41	1,78	11,71	9,92	11,06
Anodised	143	up	1,33	1,66	10,72	9,30	10,11
Anodised	144	down	1,26	1,59	10,00	8,73	9,01
Anodised	144	side 1	1,84	2,31	14,44	12,34	14,02
Anodised	144	side 2	1,46	1,89	13,86	10,50	12,36
Anodised	144	up	0,92	1,14	6,89	5,74	6,28
Anodised	145	down	1,28	1,61	10,39	9,11	9,94
Anodised	145	side 1	1,62	2,01	11,77	10,16	11,27
Anodised	145	side 2	1,66	2,06	12,35	10,98	11,80
Anodised	145	up	1,31	1,63	10,61	8,96	10,27
Anodised	146	down	1,42	1,80	13,14	10,46	12,09
Anodised	146	side 1	1,35	1,70	13,49	9,38	12,35
Anodised	146	side 2	1,27	1,63	12,15	8,96	11,47
Anodised	146	up	1,28	1,60	10,12	9,09	9,54

Sample type	Nr.	Side	Ra [µm]	Rq [µm]	Rt [µm]	Rz [µm]	Rmax [µm]
Anodised	147	down	1,35	1,69	11,50	9,54	10,82
Anodised	147	side 1	1,20	1,54	11,56	8,65	10,62
Anodised	147	side 2	1,36	1,74	10,85	9,09	10,67
Anodised	147	up	1,25	1,58	10,89	8,88	10,89
Anodised	148	down	1,40	1,77	12,37	10,01	10,67
Anodised	148	side 1	1,25	1,60	10,20	9,08	10,13
Anodised	148	side 2	1,38	1,70	10,83	8,68	10,08
Anodised	148	up	1,35	1,69	10,91	9,26	10,91
Anodised	149	down	1,29	1,65	11,84	9,23	11,30
Anodised	149	side 1	1,31	1,65	10,68	8,54	9,74
Anodised	149	side 2	1,37	1,71	10,60	9,30	10,58
Anodised	149	up	1,20	1,53	10,40	8,88	10,36
Anodised	151	down	1,16	1,47	10,17	8,19	9,13
Anodised	151	side 1	1,75	2,14	13,18	10,21	12,01
Anodised	151	side 2	1,85	2,30	14,88	12,46	13,13
Anodised	151	up	1,21	1,57	11,63	8,21	11,63
Anodised	152	down	1,37	1,77	13,78	9,53	12,89
Anodised	152	side 1	1,37	1,77	15,55	10,28	13,48
Anodised	152	side 2	1,52	1,93	12,45	10,07	12,45
Anodised	152	up	1,15	1,46	9,59	8,53	9,59
Anodised	153	down	1,37	1,71	10,83	8,82	9,57
Anodised	153	side 1	1,36	1,70	10,38	8,94	9,74
Anodised	153	side 2	1,34	1,68	11,49	9,03	10,82
Anodised	153	up	1,29	1,62	12,38	9,59	11,04
Anodised	154	down	1,25	1,56	11,41	8,80	10,28
Anodised	154	side 1	1,28	1,63	9,25	7,98	9,25
Anodised	154	side 2	1,43	1,80	12,38	9,28	11,78
Anodised	154	up	1,23	1,55	10,10	8,61	9,50
Ti Anodised	10	down	1,04	1,30	8,18	7,61	7,93
Ti Anodised	10	side 1	1,23	1,60	12,99	9,10	12,99
Ti Anodised	10	side 2	1,24	1,56	11,06	8,39	11,06
Ti Anodised	10	up	0,95	1,19	7,79	6,83	7,55
Ti Anodised	11	down	1,01	1,26	8,13	7,17	7,77
Ti Anodised	11	side 1	1,20	1,55	11,89	8,74	10,86
Ti Anodised	11	side 2	1,14	1,47	10,26	8,27	9,98
Ti Anodised	11	up	0,98	1,23	8,52	7,12	8,01
Ti Anodised	12	down	1,00	1,27	8,61	7,35	8,61
Ti Anodised	12	side 1	1,29	1,71	15,49	10,24	15,49
Ti Anodised	12	side 2	1,55	2,03	14,41	10,54	14,41
Ti Anodised	12	up	1,04	1,30	8,49	7,12	8,03
Ti Anodised	13	down	0,98	1,25	8,87	7,41	8,23
Ti Anodised	13	side 1	1,51	1,95	15,84	11,09	15,84
Ti Anodised	13	side 2	1,40	1,81	13,80	9,82	13,54
Ti Anodised	13	up	1,10	1,38	9,04	7,49	8,23
Ti Anodised	14	down	0,97	1,22	7,59	6,55	7,19
Ti Anodised	14	side 1	1,41	1,89	17,04	10,71	17,04
Ti Anodised	14	side 2	1,22	1,58	13,62	9,45	12,90
Ti Anodised	14	up	1,05	1,32	8,66	7,49	8,66

Sample type	Nr.	Side	Ra [µm]	Rq [µm]	Rt [µm]	Rz [µm]	Rmax [µm]
Ti Anodised	15	down	1,05	1,32	8,44	7,47	8,44
Ti Anodised	15	side 1	1,61	2,07	15,76	12,55	15,47
Ti Anodised	15	side 2	1,65	2,21	17,44	12,54	17,44
Ti Anodised	15	up	1,04	1,33	8,70	7,76	8,34
Ti Anodised	16	down	1,03	1,30	9,05	7,94	8,99
Ti Anodised	16	side 1	1,48	1,92	14,38	10,39	13,38
Ti Anodised	16	side 2	1,54	1,98	14,02	10,67	13,60
Ti Anodised	16	up	1,10	1,39	9,88	7,82	8,84
Ti Uncoated	1	down	0,81	1,03	8,90	6,02	8,45
Ti Uncoated	1	side 1	0,63	0,80	5,20	4,13	5,20
Ti Uncoated	1	side 2	0,61	0,78	5,22	4,47	5,12
Ti Uncoated	1	up	0,89	1,12	7,94	6,25	7,52
Ti Uncoated	2	down	0,86	1,10	8,10	6,16	7,25
Ti Uncoated	2	side 1	0,57	0,73	5,19	3,72	4,64
Ti Uncoated	2	side 2	0,72	0,91	5,87	4,55	5,87
Ti Uncoated	2	up	0,90	1,13	7,39	6,35	7,23
Ti Uncoated	3	down	0,91	1,14	8,07	6,23	7,15
Ti Uncoated	3	side 1	0,77	0,97	6,03	5,25	5,74
Ti Uncoated	3	side 2	0,56	0,72	4,67	3,83	4,67
Ti Uncoated	3	up	1,08	1,36	7,92	6,80	7,82
Ti Uncoated	5	down	0,39	0,52	5,85	3,39	5,85
Ti Uncoated	5	side 1	0,44	0,55	3,60	2,97	3,46
Ti Uncoated	5	side 2	0,48	0,59	3,42	2,97	3,35
Ti Uncoated	5	up	0,43	0,55	4,48	3,38	3,95
Ti Uncoated	6	down	0,77	0,98	8,10	6,04	6,80
Ti Uncoated	6	side 1	1,15	1,51	10,36	7,02	8,49
Ti Uncoated	6	side 2	0,58	0,72	4,60	3,75	4,51
Ti Uncoated	6	up	0,89	1,20	9,73	6,71	9,52
Ti Uncoated	7	down	0,70	0,89	6,06	5,19	5,62
Ti Uncoated	7	side 1	1,00	1,31	8,53	6,27	7,95
Ti Uncoated	7	side 2	0,61	0,76	5,77	3,96	5,77
Ti Uncoated	7	up	0,88	1,13	8,98	6,31	8,21
Ti Uncoated	8	down	0,95	1,24	9,84	7,00	8,68
Ti Uncoated	8	side 1	0,79	1,00	6,62	5,63	6,12
Ti Uncoated	8	side 2	0,69	0,86	5,90	4,49	5,28
Ti Uncoated	8	up	0,97	1,29	11,19	7,50	10,26
Ti Uncoated	9	down	0,70	0,89	6,68	5,35	6,44
Ti Uncoated	9	side 1	0,67	0,87	6,34	4,64	6,34
Ti Uncoated	9	side 2	0,80	1,02	7,66	5,77	7,58
Ti Uncoated	9	up	0,66	0,85	8,29	5,03	7,93